ATMOSPHERIC CORRECTION OVER OCEAN

FOR PRODUCTION OF REMOTE SENSING REFLECTANCE INTERMEDIATE PRODUCT

VISIBLE/INFRARED IMAGER/RADIOMETER SUITE ALGORITHM THEORETICAL BASIS DOCUMENT

Version 5: March 2002

Quanhua Liu
Corinne Carter

Kendal Carder, Science Team Member
University of South Florida

RAYTHEON SYSTEMS COMPANY
Information Technology and Scientific Services
4400 Forbes Boulevard
Lanham, MD 20706

SBRS Document #: Y2389

SDR: ATMOSPHERIC CORRECTION OVER OCEAN

Doc No: Y2389

Version: 5

Revision: 0

	FUNCTION	NAME	SIGNATURE	DATE
Prepared By	EDR Developer	Q. LIU		1/25/02
Approved By	Relevant IPT Lead	D. HOMMEL		2/1/02
Approved By	Chief Scientist	S. MILLER		2/8/02
Released By	Algorithm IPT Lead	P. KEALY		2/15/02

TABLE OF CONTENTS

Page

TABLE OF CONTENTS i

LIST OF FIGURES iii

LIST OF TABLES v

GLOSSARY OF ACRONYMS vii

ABSTRACT ix

1.0 INTRODUCTION 1

1.1 PURPOSE 1
1.2 SCOPE 1
1.3 VIIRS DOCUMENTS 1
1.4 REVISIONS 1

2.0 EXPERIMENT OVERVIEW 3

2.1 OBJECTIVES OF ATMOSPHERIC CORRECTION OVER OCEAN 3
2.2 INSTRUMENT CHARACTERISTICS 3
2.3 RETRIEVAL STRATEGY 4

3.0 ALGORITHM DESCRIPTION 5

3.1 PROCESSING OUTLINE 5
3.2 ALGORITHM INPUT 5
3.2.1 VIIRS Data 5
3.2.2 Non-VIIRS Data 5
3.3 THEORETICAL DESCRIPTION OF ATMOSPHERIC CORRECTION OVER OCEAN RETRIEVALS 5
3.3.2 Mathematical Description of the Algorithm 8
3.3.3 Diffuse Transmittance 10
3.3.4 Aerosol effect 10
3.3.5 Sun glint mask and correction 15
3.3.6 Algorithm Output 16
3.3.7 Variance and Uncertainty Estimates 16
3.4 ALGORITHM SENSITIVITY STUDIES 18
3.4.1 Calibration Errors 18
3.4.2 Instrument Noise 18
3.4.3 Stray light effect 22
3.4.4 Residual instrumental polarization 27
3.4.5 Absorbing aerosols 33
3.5 PRACTICAL CONSIDERATIONS 34
3.5.1 Numerical Computation Considerations 34
3.5.2 Correction to the Instrumental Polarization 34

3.5.3 Stray Light Warning Flag 35
3.5.4 Programming and Procedural Considerations.....35
3.5.5 Quality Assessment and Diagnostics 35
3.5.6 Exception Handling.....36
3.5.7 Masks and Flags.....36
3.6 ALGORITHM VALIDATION.....36
3.6.1 Error Budget.....36
3.6.2 Global maps of remote sensing reflectance and retrieval of chlorophyll 37
3.6.3 Post-launch validation.....38
3.7 ALGORITHM DEVELOPMENT ACTIVITIES (P^3I).....39

4.0 ASSUMPTIONS AND LIMITATIONS 41

4.1 ASSUMPTIONS.....41
4.2 LIMITATIONS.....41

5.0 ACKNOWLEDGEMENTS.....43

6.0 REFERENCES.....45

LIST OF FIGURES

Page

Figure 1. VIIRS band position and width. Solid line represents the Rayleigh optical thickness. The dashed line indicates the optical thickness of gases. In this figure, the right-hand dark box represents the old band centered at 751 nm, which was later adjusted to reduce the influence of the adjacent O_2 absorption feature.....4

Figure 2. Algorithm flow diagram adapted from Gordon (1996).....6

Figure 3. Simulated TOA radiance from the modified MODTRAN radiative transfer model. The light gray part represents the atmospheric contribution. The gray part is the contribution from air-sea interface. The dark gray indicates the water-leaving radiance.....7

Figure 4. Spectral variation of the water-leaving radiances measured by the high-resolution spectrographs on MOBY. 8

Figure 5. Schematic drawing of the radiation transport. 11

Figure 6. Comparison of the Rayleigh diffuse transmittance from the analytic approximation and the detailed radiative transfer calculation.....11

Figure 7a. Comparison of the diffuse transmittance from our derivation and the detailed radiative transfer calculation.....12

Figure 7b. Variation of the phase function with the scattering angle.....13

Figure 7c. Values of $\varepsilon(\lambda,\lambda858)$ for nadir viewing with $\theta_0=60^0$ for the maritime, costal, and tropospheric aerosol models. For each model, the relative humidity values are 50, 70, 90, and 99% from the top to the bottom curves.....14

Figure 8. Sun glint (red color) area for a wind speed of 8 m s^{-1} for simulated 1330 VIIRS orbit.....15

Figure 9. Sun glint probability contours (solid) for a sea surface wind speed of 5 m s^{-1} and sun zenith of 30°. 16

Figure 10. Mean chlorophyll precision due to sensor noise in the VIIRS near-IR bands as a function of VIIRS sensor performance model number. The precision values are averages for a 2400 km wide swath and solar zenith angle less than 70 degrees. The dashed line indicates the threshold requirement of 20 percent. The numbers on the x- axis represent models with worsening signal to noise ratio as the sensor model number increases. The Raytheon VIIRS final sensor noise level is between that given by sensor models 2 and 3.....20

Figure 11. Mean chlorophyll precision due to sensor noise in the VIIRS visible bands as a function of VIIRS sensor performance model number. The precision values are averages for a 2400 km wide swath and solar zenith angle less than 70 degrees. The dashed line indicates the threshold requirement of 20 percent. The numbers on the x- axis represent models with worsening signal to noise ratio as the

sensor model number increases. The Raytheon VIIRS final sensor is between that given by sensor models 2 and 3. 21

Figure 12. Chlorophyll precision due to sensor noise, averaged over the viewing swath of the 1:30 PM orbit, as a function of VIIRS sensor performance model. The results for atmospheric correction using the 745-785 nm and 841-876 nm band pair are shown as diamonds. The results using the 743-753 nm and 841-876 nm band pair are shown as crosses. 21

Figure 13. Chlorophyll accuracy as a function of a distance from the edge of a semi-infinite cloud. A dashed line represents the accuracy of 10% allocated for the stray light error source. 24

Figure 14. Comparison of the chlorophyll accuracy obtained with no atmospheric correction and the Gordon-Wang atmospheric correction algorithm. A dashed line represents the accuracy of 10% allocated for the stray light error source. 25

Figure 15. Comparison of the chlorophyll accuracy calculated for a semi-infinite cloud, desert, and vegetation. The Gordon-Wang atmospheric correction algorithm was applied to the TOA radiances..... 26

Figure 16. Comparison of the chlorophyll accuracy calculated for the semi-infinite and limited clouds using the Gordon-Wang atmospheric correction. 27

Figure 17. Degree of polarization at 443 nm. 30

Figure 18. Variation of linear polarization with the optical depth of the aerosol. 31

Figure 19. Sun zenith = 41 degree, viewing = 30 degree, Relative azimuth = 90 degree, chlorophyll = 0.1 mg/m3..... 32

Figure 20. Retrieval uncertainty for various polarization sensitivities. The two-step algorithm yields the best results. 33

Figure 21. Variation of $\varepsilon(\lambda, 865)$ for nadir viewing with a sun zenith angle of 41° for the maritime, continental and urban aerosol models for RH=50% and a desert aerosol (wintertime) with RH=0%. 34

Figure 22. Retrieved remote sensing reflectance. 37

Figure 23.Uncertainty of the retrieval of the chlorophyll concentration. 38

LIST OF TABLES

Page

Table 1. VIIRS Visible and Near-infrared Bands 3

Table 2. Processing Speeds for Preliminary Implementation of the Atmospheric Correction Algorithm for SeaWiFS 35

GLOSSARY OF ACRONYMS

3-D	Three-dimensional
6S	Second Simulation of the Satellite Signal in the Solar Spectrum
ATBD	Algorithm Theoretical Basis Document
EDR	Environmental Data Record
MM5	Mesoscale Model, version 5
MOBY	Marine Optical Buoy
MODIS	Moderate Resolution Imaging Spectroradiometer
MODTRAN	Moderate Resolution Atmospheric Radiance and Transmittance Model
NIR	Near-Infrared
OMPS	Ozone Mapping Profiling Suite
SeaWiFS	Sea-viewing, Wide Field-of-view Sensor
TBD	To Be Determined
TOA	Top of Atmosphere
VIIRS	Visible/Infrared Imager/Radiometer Suite

ABSTRACT

This Algorithm Theoretical Basis Document (ATBD) describes the atmospheric correction algorithm developed by Gordon and Wang (1994a) for use on Sea-viewing, Wide Field-of-view Sensor (SeaWiFS) and Moderate Resolution Imaging Spectroradiometer (MODIS) data. A polarized radiative transfer model extends the algorithm, accounting for the residual instrumental polarization sensitivity. Inputs to the algorithm are measured Visible/Infrared Imager/Radiometer Suite (VIIRS) radiances in the visible and near-infrared bands, sea surface wind speed, surface atmospheric pressure, and total ozone column. The algorithm subtracts the contributions of molecular and aerosol scattering in the atmosphere, and reflection from the air-sea interface, from the measured VIIRS radiances. It includes effects of single and multiple scattering and whitecap reflectance, and is applied only under clear-sky daytime conditions. Major sources of uncertainty in the retrieved water-leaving reflectances are: (1) the possibility that the candidate aerosol models may not be representative of some regions; (2) the assumption of zero water-leaving radiance in two near-infrared bands may not be valid for regions with high chlorophyll or coccolith concentration or turbid water; (3) uncertainty in whitecap reflectance; (4) uncertainty in VIIRS radiometric calibration, polarization sensitivity, and sensor noise. This algorithm produces the VIIRS Remote Sensing Intermediate Product (IP), which is an input to the VIIRS Ocean Color/Chlorophyll unit.

1.0 INTRODUCTION

1.1 PURPOSE

This Algorithm Theoretical Basis Document (ATBD) describes the algorithm used to produce the VIIRS Remote Sensing Reflectance IP, which consists of water-leaving remote sensing reflectances in each of five visible-wavelength VIIRS bands. This information is used by bio-optical algorithms in the retrieval of the VIIRS Ocean Color/ Chlorophyll Environmental Data Record (EDR). The algorithm operates on the assumption that the signal in the near infrared is due entirely to the atmosphere, which is a reasonable assumption for non-turbid waters and open ocean.

1.2 SCOPE

This document covers the algorithm theoretical basis for retrieval of water-leaving reflectances. Section 1 describes the purpose and scope of the document. Section 2 provides an overview of the uses of water-leaving reflectance retrievals and lists relevant VIIRS instrument characteristics. Section 3 describes the algorithm, practical aspects of its operation, results of sensitivity studies, and methods of validation. Section 4 summarizes assumptions and limitations of the algorithm. References for publications cited are given in Section 5.

1.3 VIIRS DOCUMENTS

References to VIIRS documents are indicated by a number in italicized brackets, e.g., *[V-1]*.

[V-1] VIIRS Flowdown Results: Radiometric Noise Requirements for Chlorophyll, RAD.NEDL.OC, 1998.

[Y-2408] VIIRS Algorithm Theoretical Basis Document for Ocean Color, Version 5, March 2002.

[Y-3249] VIIRS Error Budget, Version 3, April 2000. Appendix A of VIIRS Phase I System Verification Report.

[Y-3257] VIIRS Computer Resource Requirements.

1.4 REVISIONS

This is the fifth version of the algorithm theoretical basis document for the atmospheric correction over ocean. The first version of the document was written by Odegard and Vasilkov, dated October 1998. The second version of the document, dated June 1999, was developed through revisions and extensions to the first version by Liu, Odegard, Vasilkov, and Wang. Liu et al. extended the second version to create the third version of this document in May 2000.

The fourth version, written in May 2001, includes updated information on sensor characteristics in Table 1, a new sub-section to address masks and flags, and the spectrally dependent reflectance of whitecaps. The changes made for this version (Version 5, January 2002) include the new sub-section 3.3.5 for the sun glint mask. The correction to the instrumental polarization

is given in the new sub-section 3.5.2. Stray light and the warning flag for stray light are addressed in the new sub-section 3.5.3. The use of a 3D radiative transfer model to study stray light and using the OMPS UV index for absorbing aerosols are discussed as potential P^3I activities. (see new sub-section 4.3).

2.0 EXPERIMENT OVERVIEW

2.1 OBJECTIVES OF ATMOSPHERIC CORRECTION OVER OCEAN

The goal of atmospheric correction over the ocean is to remove the contributions of scattering in the atmosphere and reflection from the sea surface from the top-of-atmosphere radiances measured by a sensor in the visible region of the spectrum. The quantity retrieved is water-leaving remote sensing reflectance, which is used in retrieval of the Ocean Color/ Chlorophyll EDR. Water-leaving reflectance is at most 10 percent of the top-of-atmosphere (TOA) reflectance in the visible part of the spectrum (Gordon and Morel, 1983), so accurate atmospheric correction is required. The algorithm is applied under clear-sky daytime conditions for deep-water pixels that are not affected by sun glint. For a shallow-water pixel it may be reasonable to assume that the atmospheric contribution determined for the nearest deep-water pixel is valid. Otherwise, a special atmospheric correction algorithm for the application is required.

2.2 INSTRUMENT CHARACTERISTICS

Table 1 lists central wavelengths and bandwidths for the VIIRS visible and near-infrared bands as well as representative values of TOA radiance above the ocean, L_{typ}. The L_{typ} values match those adopted by MODIS. It is recognized that the SeaWiFS NIR band at 765 is strongly affected by O_2 absorption, which complicates corrections for thin cirrus clouds. To avoid the strong oxygen absorption, the Raytheon VIIRS NIR band is centered at 746 nm with a width of 15 nm.

Table 1. VIIRS Visible and Near-infrared Bands

Wavelength (nm)	Bandwidth (nm)	L_{typ} (W m^{-2} µm^{-1} sr^{-1})
412	20	44.9
445	18	40
488	20	32
555	20	21
672	20	10
746	15	9.6
865	39	6.4

The I1 red band, at 620 – 670 nm, is contaminated by the water vapor absorption. The water vapor absorption is difficult to account for correctly, because water vapor is the most variable gas in the atmosphere. The moderate resolution red band was finally located at 672 nm with a band width of 20 nm to avoid the water vapor absorption. It can be seen from Figure 1 that the Raytheon band configuration is optimized to reduce the water vapor absorption and to avoid the oxygen absorption. The second NIR band is the heritage SeaWiFS band.

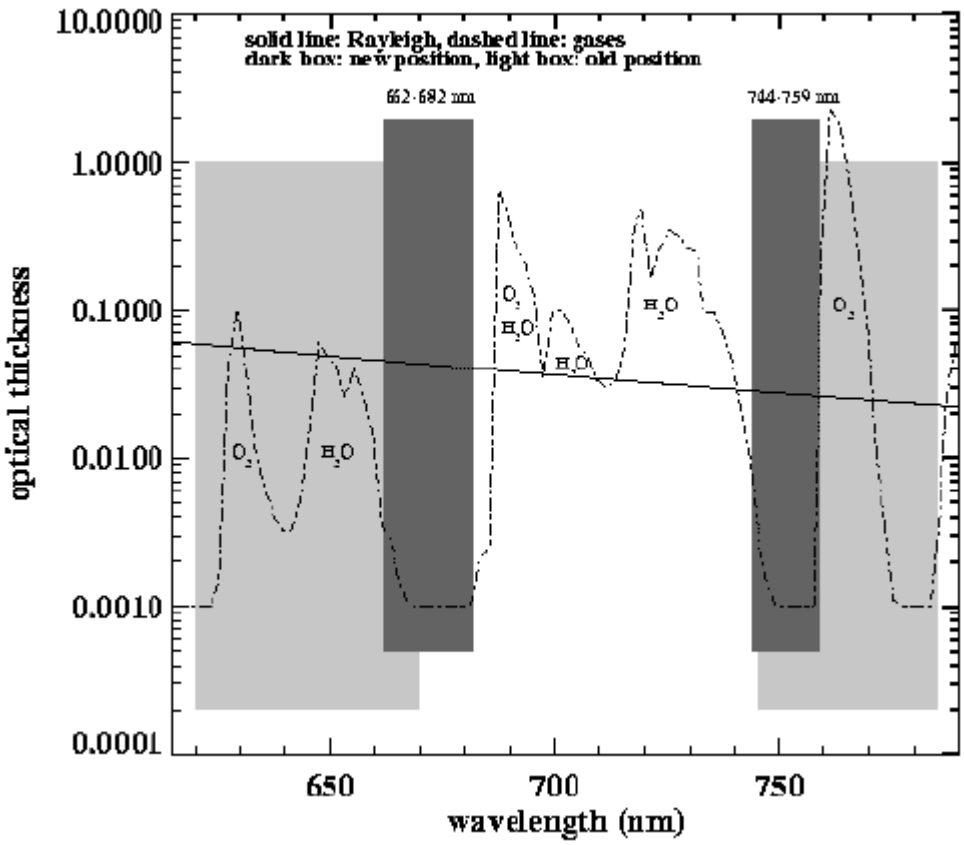

Figure 1. VIIRS band position and width. Solid line represents the Rayleigh optical thickness. The dashed line indicates the optical thickness of gases. In this figure, the right-hand dark box represents the old band centered at 751 nm, which was later adjusted to reduce the influence of the adjacent O_2 absorption feature.

2.3 RETRIEVAL STRATEGY

Atmospheric correction retrievals will be performed only under clear sky, daytime conditions for deep-water regions that have no ice cover and are not affected by sun glint. If a cloud mask, shallow water mask, ice cover mask, or sun glint mask is not set for a given pixel, atmospheric correction of VIIRS top-of-atmosphere radiances is performed. To perform atmospheric correction, non-VIIRS data sets such as total ozone amount and sea surface wind are needed. The output of the atmospheric correction algorithm is water-leaving reflectance or remote sensing reflectance, which is an input to the ocean color/ chlorophyll algorithm. Currently, the atmospheric correction algorithm over shallow water or turbid water can only be performed by "borrowing" the correction over the nearest deep water.

3.0 ALGORITHM DESCRIPTION

3.1 PROCESSING OUTLINE

Figure 2 presents a schematic flowchart for the Gordon-Wang algorithm, adapted from Gordon (1996). The radiance L_m measured at the top of the atmosphere in each of the visible to near-infrared bands is divided by the extraterrestrial solar irradiance F_0 to obtain the measured reflectance ρ_m. The reflectance contributed by whitecaps is estimated from the surface wind speed W and subtracted from ρ_m. Corrections for ozone absorption are applied to obtain the reflectance ρ_t. The surface atmospheric pressure P and wind speed are used to compute the Rayleigh reflectance ρ_r, which is subtracted from ρ_t. The algorithm then selects from a family of aerosol models to fit the residual reflectance ρ_t-ρ_r in the 751 and 865 nm bands, assuming that the water-leaving reflectance in each of these bands is zero. It interpolates between selected aerosol models to obtain an exact fit to ρ_t-ρ_r at 751 and 865 nm, and to estimate the aerosol contribution in each of the visible wavelength bands. After subtraction of the aerosol contribution, the water-leaving reflectance is obtained in each of the visible bands by dividing by the diffuse atmospheric transmittance.

3.2 ALGORITHM INPUT

3.2.1 VIIRS Data

The algorithm uses band-averaged spectral reflectances measured at the top of the atmosphere in each of the VIIRS visible and near-infrared bands. These band-averaged reflectances can be used because VIIRS is calibrated in reflectance units directly.

3.2.2 Non-VIIRS Data

The algorithm takes calibrated reflectances from the VIIRS SDR, then uses the ozone total column to correct for ozone absorption, precipitable water to correct for water vapor absorption, surface atmospheric pressure to calculate Rayleigh optical depth, and surface wind velocity (speed and direction). The wind speed is used to correct for whitecap reflectance (Frouin et al., 1996) and to calculate Rayleigh reflectance, and the wind velocity is used to construct a sun glint mask. Data such as the absorbing aerosol index from the Ozone Mapping Profiling Suite (OMPS) may also be used in a future version of the algorithm for handling pixels with strongly absorbing aerosols.

3.3 THEORETICAL DESCRIPTION OF ATMOSPHERIC CORRECTION OVER OCEAN RETRIEVALS

Physics of the Problem

The reflectance backscattered from the atmosphere and/or sea surface is typically at least an order of magnitude larger than the desired radiance scattered out of the water. The contribution of the water-leaving reflectance to the TOA reflectance decreases with the increase of the viewing angle because of the reduction of the diffuse transmittance. The process of retrieving water-leaving reflectance from the total reflectance measured at the sensor is usually referred to as atmospheric

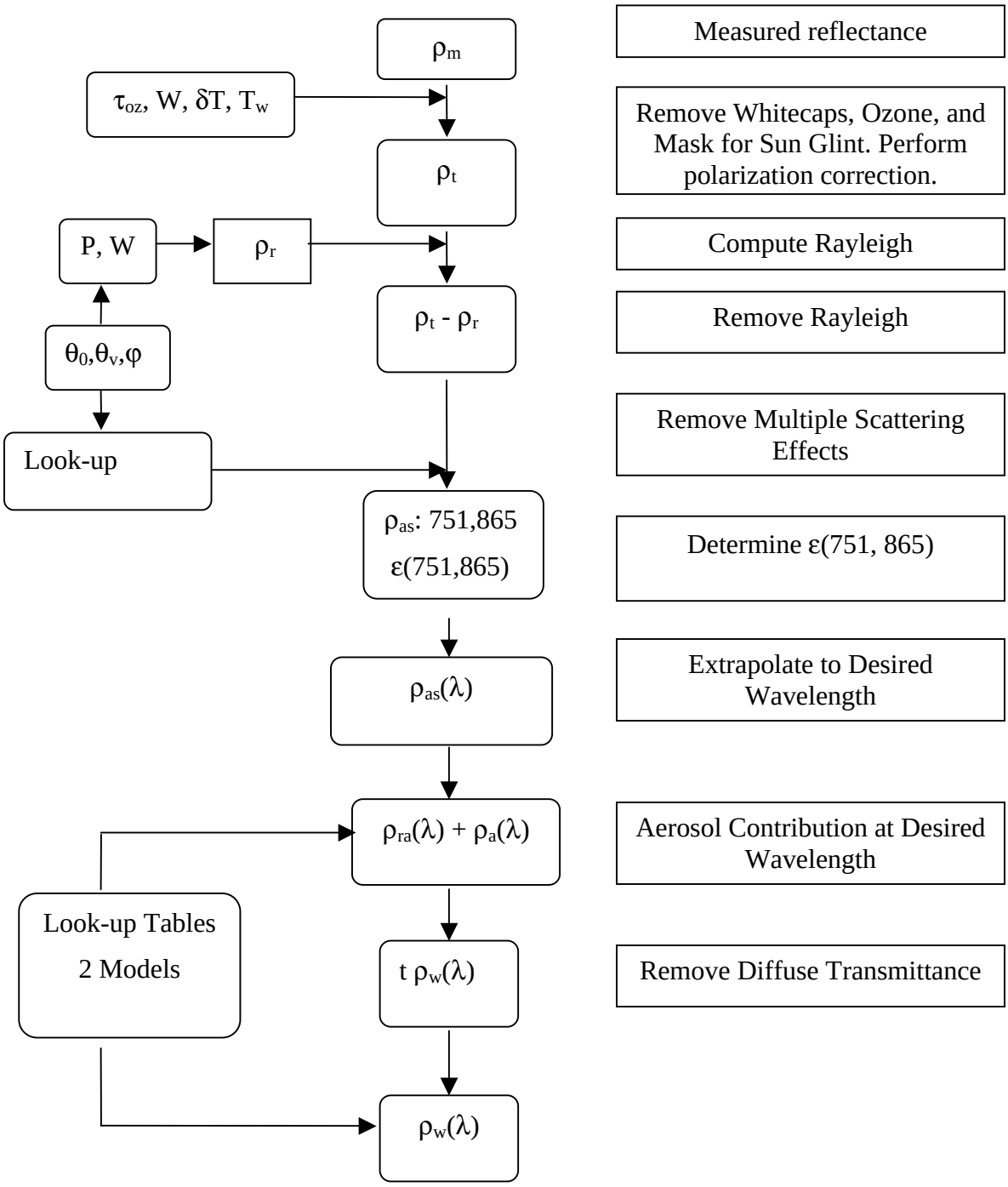

Figure 2. Algorithm flow diagram adapted from Gordon (1996).

correction, even though all surface reflection effects other than direct sun glint are removed with a single algorithm. Atmospheric effects are principally due to Rayleigh scattering and scattering by aerosol particles. These effects could be accurately removed if the concentration and optical properties of the aerosol were known. However, these aerosol properties are highly variable in position and time, and the aerosol contribution to the measured radiance at TOA cannot be predicted *a priori*. Therefore, atmospheric correction must be performed for each observation of each pixel, using the measurements themselves to determine the aerosol contribution. A major difficulty of atmospheric correction over the ocean is that the atmospheric and surface reflectance contributions to be removed from the top-of-atmosphere reflectance are much greater than the water-leaving reflectance contribution. Figure 3 shows the simulated signal of the TOA radiance from the atmosphere, air-sea interface, and water-leaving radiance. It is clear that the atmospheric correction removes a large signal and keeps a very small signal from the water.

The two NIR bands can be used to derive aerosol information since they depend only on the atmospheric state and the reflection of air-sea interface for most water. Surface measurements (Herring 1997) show that the water-leaving radiance at NIR bands is negligible (see Figure 4). It should be pointed out that the ratio of the signal to noise is a key factor affecting the selection of the aerosol model and the calculation of the diffuse transmittance, which convert the water-leaving reflectances to the remote sensing reflectances.

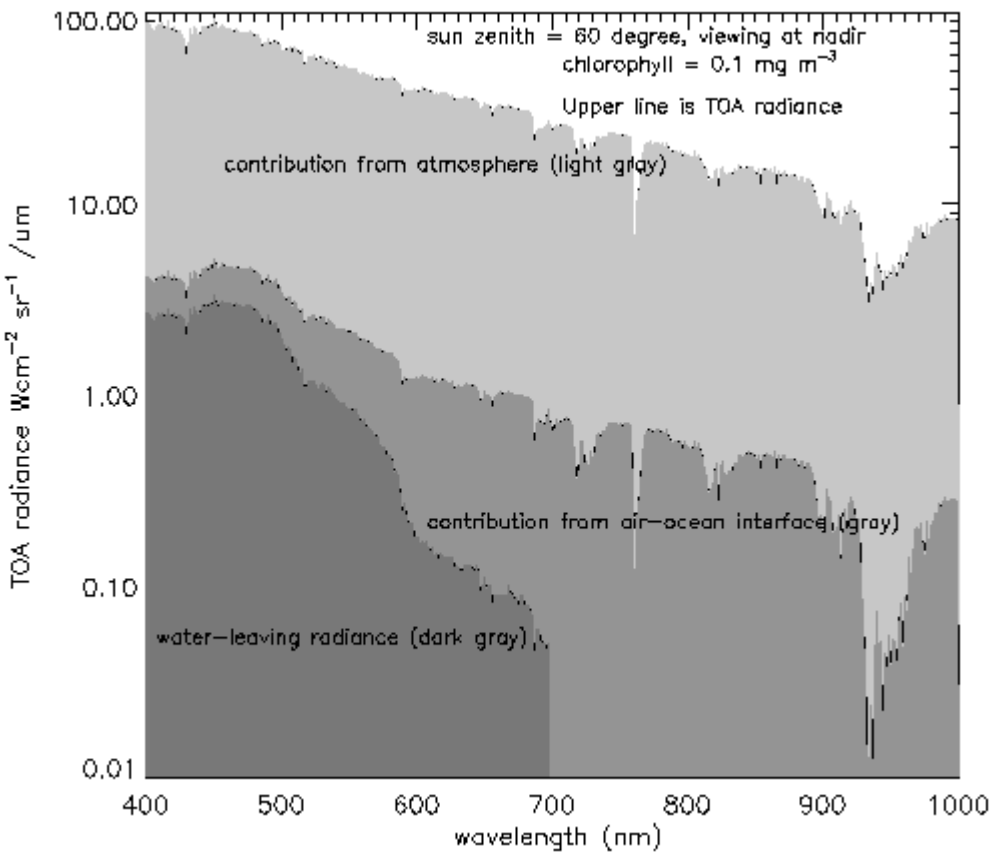

Figure 3. Simulated TOA radiance from the modified MODTRAN radiative transfer model. The light gray part represents the atmospheric contribution. The gray part is the contribution from air-sea interface. The dark gray indicates the water-leaving radiance.

3.3.2 Mathematical Description of the Algorithm

The upward radiance at the top of the atmosphere over the ocean is composed of the atmosphere-scattered radiance, air-sea interface reflected radiance, and transmitted water-leaving radiance (see Figure 5).

The algorithm has been described in detail by Gordon (1996, 1997a); only a summary is presented here. The ocean-viewing radiance can be written as:

$$L_m(\lambda) = L_{path}(\lambda) + T(\theta_v,\lambda)\, L_g(\lambda) + t(\theta_v,\lambda)\, L_{wc}(\lambda) + t(\theta_v,\lambda)\, L_w(\lambda) \qquad (1)$$

Here L_{path} is the radiance originating along the optical path from scattering in the atmosphere and from specular reflection of scattered light (skylight) by the sea surface, L_g is the radiance originating from specular reflection of direct sunlight by the sea surface (sun glitter), L_{wc} is the radiance originating from reflection of direct sunlight and skylight from whitecaps, and L_w is the water-leaving radiance from whitecap-free areas of the surface. $T(\theta_v)$ and $t(\theta_v)$ are the direct transmittance and the diffuse transmittance, respectively, of the atmosphere along the path from the ocean surface to the sensor. The path radiance can be decomposed into three components:

$$L_{path}(\lambda) = L_r(\lambda) + L_a(\lambda) + L_{ra}(\lambda) \qquad (2)$$

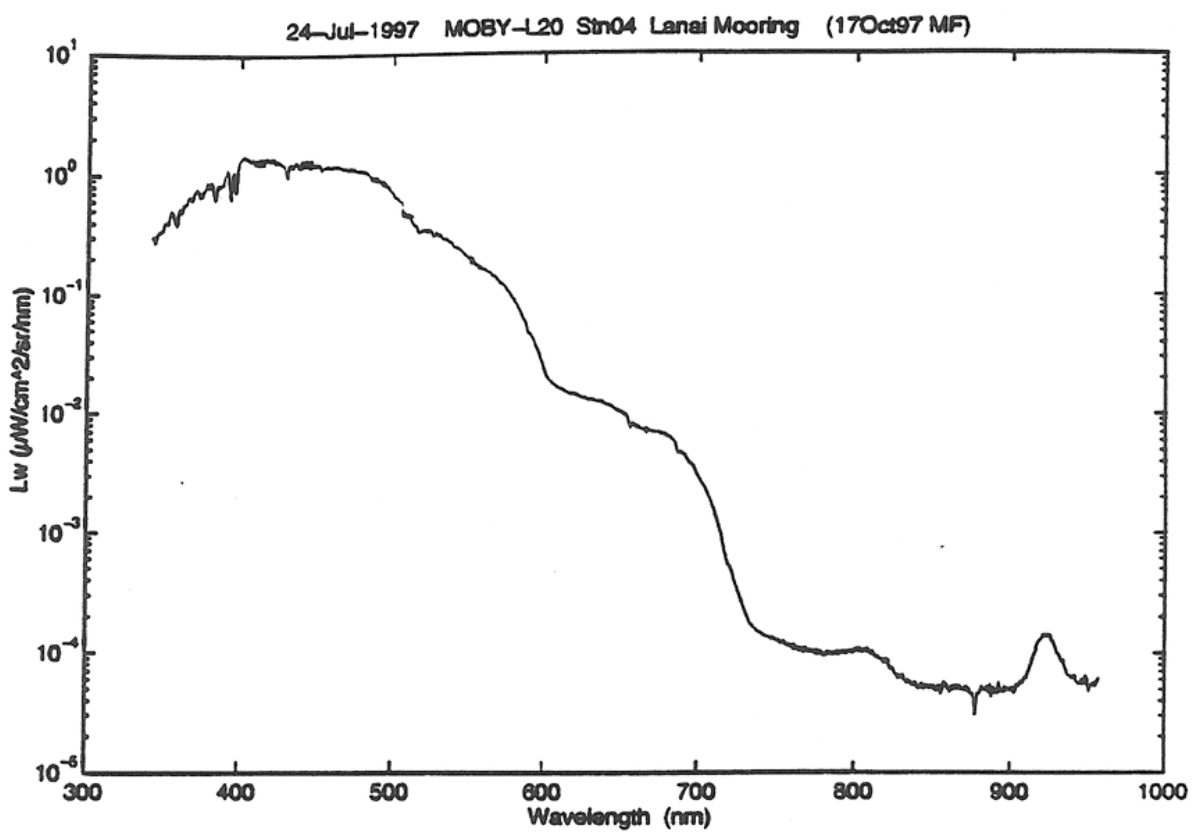

Figure 4. Spectral variation of the water-leaving radiances measured by the high-resolution spectrographs on MOBY.

where L_r is the radiance originating from single and multiple scattering by air molecules (Rayleigh scattering), L_a is the radiance originating from single and multiple scattering by aerosols, and L_{ra} is the radiance originating from multiple scattering events involving both Rayleigh and aerosol scattering. Combining equations (1) and (2), and converting to reflectance ρ using the definition $\rho \equiv \pi L/(F_0 \cos\theta_0)$, where F_0 is the extraterrestrial solar irradiance and θ_0 is the solar zenith angle, yields:

$$\rho_m(\lambda) = \rho_r(\lambda) + \rho_a(\lambda) + \rho_{ra}(\lambda) + T(\theta_v,\lambda)\, \rho_g(\lambda) + t(\theta_v,\lambda)\, \rho_{wc}(\lambda) + t(\theta_v,\lambda)\, \rho_w(\lambda) \qquad (3)$$

The goal of the atmospheric correction algorithm is to retrieve the water-leaving reflectance ρ_w in each of the VIIRS visible wavelength bands. A sun glint mask is used to discard data for viewing geometries where the sun glint contribution is significant. The mask is constructed based on ancillary wind velocity data and the Cox and Munk (1954) model of the sea surface. The whitecap contribution is small and can be estimated using:

$$\rho_{wc}(\lambda) = 6.49 \times 10^{-7}\, fwc(\lambda) \times W^{3.52}\, t(\theta_0,\lambda) \qquad (4)$$

where $fwc(\lambda)$ is a function expressing the spectral dependence of whitecap reflection, W is wind speed in m s^{-1}, $t(\theta_0,\lambda)$ is the diffuse transmittance along the path from the sun to the ocean surface (Koepke, 1984; Gordon and Wang, 1994b).The spectral-dependence of the reflectance due to whitecaps is adopted from the work of Frouin et al. (1996). The Rayleigh scattering contribution ρ_r can be calculated accurately, including polarization effects, from ancillary surface atmospheric pressure data and surface wind speed data (Gordon et al., 1988; Gordon and Wang, 1992).

The contribution involving aerosol scattering, $\rho_A \equiv \rho_a + \rho_{ra}$, cannot be determined accurately from available ancillary data. Its magnitude and wavelength dependence can vary greatly with position and time, due to variations in aerosol concentration and aerosol optical properties. The Gordon-Wang algorithm makes the assumption that $\rho_w = 0$ in the two near-infrared bands (751 and 865 nm), so the aerosol contribution in these bands is given by $\rho_A = \rho_m - \rho_r - t\, \rho_{wc}$. The algorithm then selects from a family of aerosol models to fit the aerosol contribution in the near-infrared bands and to estimate the aerosol contribution in the visible bands. The family of models includes the tropospheric and maritime aerosol models of Shettle and Fenn (1979) and a coastal aerosol model. The maritime model consists of 99 percent tropospheric and 1 percent oceanic aerosols, and the coastal aerosol model, introduced by Gordon and Wang (1994a), consists of 99.5 percent tropospheric aerosols and 0.5 percent oceanic aerosols. The tropospheric and oceanic components of these models are specified by particle size distributions and refractive indices that vary as a function of relative humidity. The algorithm makes use of Mie theory to calculate look-up tables for each aerosol model, giving $\rho_A(\lambda)$ for different relative humidity values, different aerosol concentrations, and different solar and viewing geometries. The radiative transfer calculations are done for a two-layer plane parallel atmosphere bounded by a smooth Fresnel-reflecting ocean surface, with all aerosol scattering occurring in the lower layer and all Rayleigh scattering occurring in the upper layer. Effects of multiple scattering are included, but polarization effects are not included. The different aerosol models used are thought to be representative of aerosols present over the oceans; none of the models are appropriate for strongly absorbing aerosols such as desert dust or urban pollution.

After subtraction of the whitecap, Rayleigh, and aerosol contributions from ρ_m, division by the diffuse transmittance is required to obtain water-leaving reflectance ρ_w. The diffuse transmittance is given approximately by:

$$t(\theta_v,\lambda) = \exp[-\{ \tau_r(\lambda)/2 + \tau_{Oz}(\lambda) + [1- \omega_{as}(\lambda) F(\theta_v,\lambda)] \tau_{as}(\lambda) \}/\cos \theta_v] \quad (5)$$

where τ_r, $\tau_{Oz,}$ and τ_{as} are Rayleigh, ozone, and aerosol optical depth, respectively, ω_{as} is the aerosol single-scattering albedo, F is the aerosol forward scattering probability, and θ_v is the sensor viewing zenith angle (Gordon et al., 1983). The diffuse transmittance depends primarily on the Rayleigh and ozone optical depth, which are accurately known from surface atmospheric pressure and total ozone data; it also depends to a limited extent on aerosol attenuation. Look-up tables will be produced to provide the aerosol attenuation term for the aerosol models selected by the algorithm.

The algorithms that have been adopted for retrieval of the VIIRS Ocean Color/Chlorophyll EDR make use of remote-sensing reflectance R_{rs}, the ratio of water-leaving radiance to downwelling irradiance just above the sea surface. R_{rs} values can be determined from:

$$R_{rs}(\lambda) = \rho_w(\lambda)/[\pi\, t(\theta_0,\lambda)] \quad (6)$$

3.3.3 Diffuse Transmittance

Equation 5 for calculating diffuse transmittance is an approximate form. The approximation can give an error of 2 - 4% even for the Rayleigh scattering only. Figure 7 shows the results of the Rayleigh diffuse transmittance from a detailed model calculation and from Equation 5. We have developed an accurate method to calculate the diffuse transmittance. Our derived diffuse transmittance agrees very well with the detailed radiative transport calculation (see Figure 7a).

3.3.4 Aerosol effect

The Rayleigh scattering effect can be easily removed because its phase function is a well-known analytic function and its optical thickness can be calculated according to the surface pressure. The aerosol effect, however, is a more uncertain component of the atmospheric correction. Different aerosols have different behavior, especially absorbing aerosols. The particle size of aerosol grows with increasing relative humidity. It can be seen from Figure 7b that the phase function of aerosols depends on the aerosol type as well as the relative humidity. The single scattering approach is the basis of the present method for selecting aerosol models; it is a good approximation because of the low optical thickness of the aerosols over the ocean. The single scattering effect for small optical thickness is a product of the single scattering albedo, phase function, and optical thickness. It is known that the ratio of this product at two wavelengths is approximately an exponential function (see Figure 7c). In principle, radiances at two NIR bands can determine one straight line in the plane epsilon-wavelength. However, sensor noise and algorithm error could prevent a correct selection of the aerosol model. Therefore, radiometric noise is an issue for the atmospheric correction over ocean. The combination of the red band at 672 nm and the NIR band at 865 nm may have an advantage for the atmospheric correction in some cases because of the large difference between the wavelengths of the two bands.

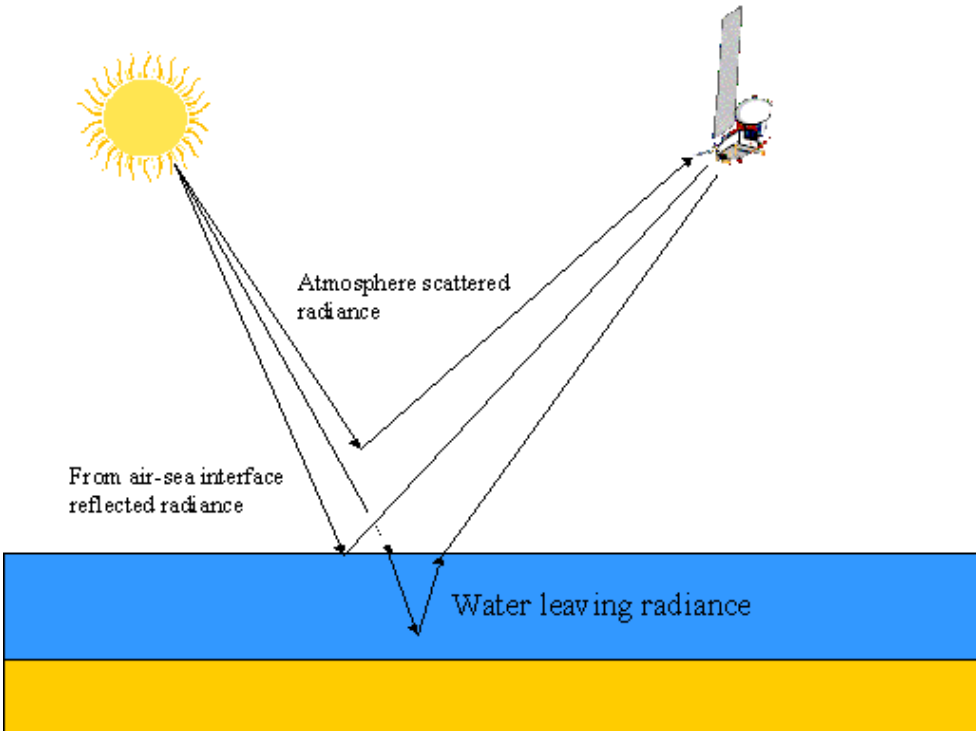

Figure 5. Schematic drawing of the radiation transport.

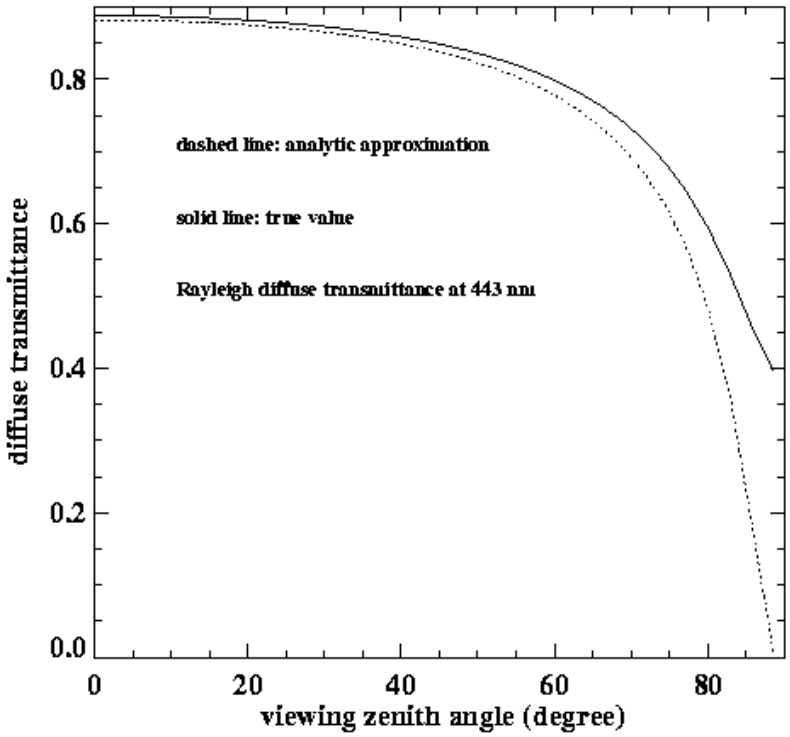

Figure 6. Comparison of the Rayleigh diffuse transmittance from the analytic approximation and the detailed radiative transfer calculation

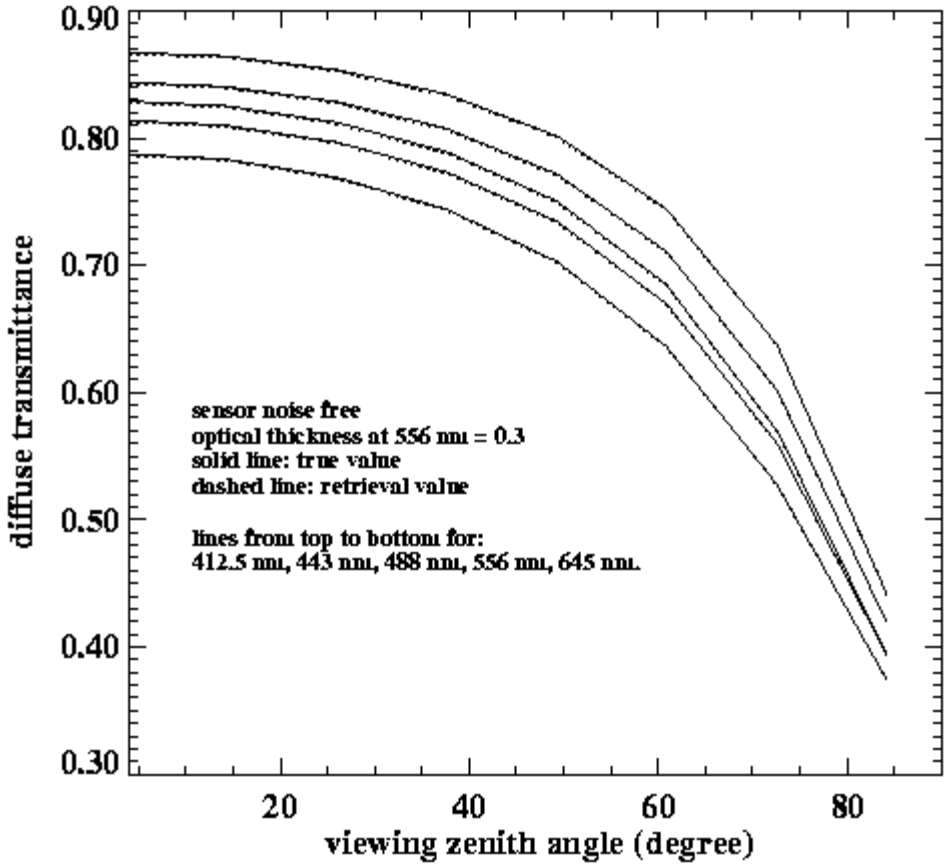

Figure 7a. Comparison of the diffuse transmittance from our derivation and the detailed radiative transfer calculation.

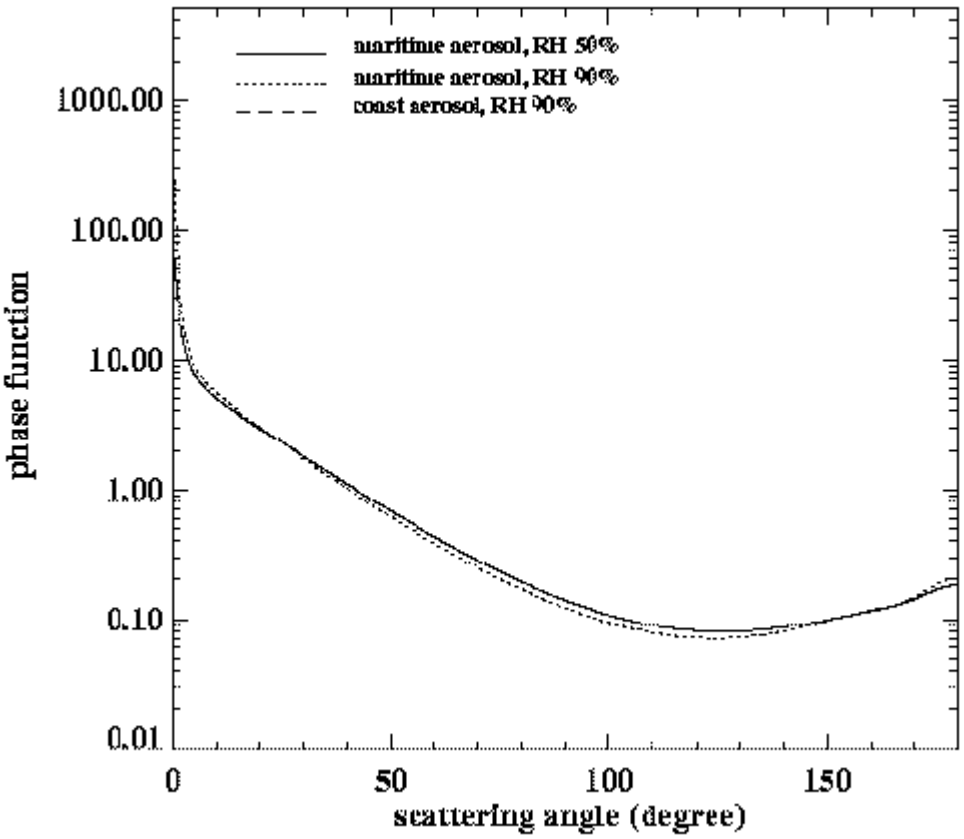

Figure 7b. Variation of the phase function with the scattering angle.

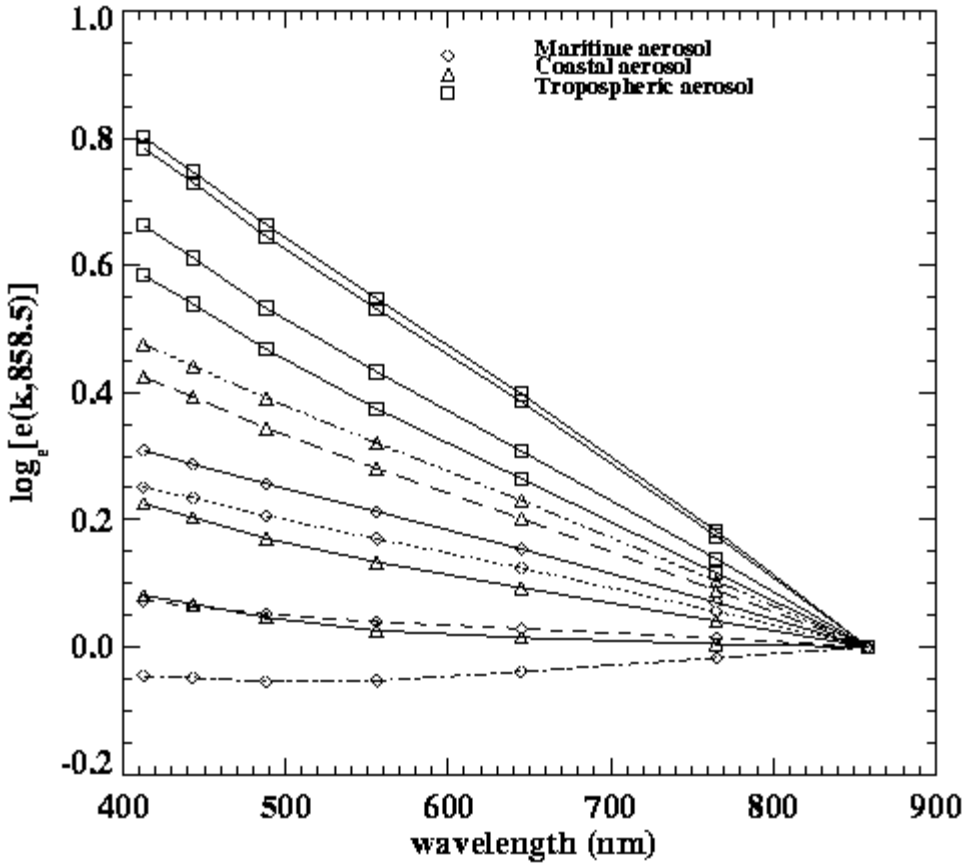

Figure 7c. Values of $\varepsilon(\lambda,\lambda 858)$ for nadir viewing with $\theta_0=60^0$ for the maritime, costal, and tropospheric aerosol models. For each model, the relative humidity values are 50, 70, 90, and 99% from the top to the bottom curves.

3.3.5 Sun glint mask and correction

Sun glint refers to the phenomenon of incoming solar radiation directly reflected from the ocean surface to the sensor. For an absolutely flat ocean surface, the sun glint occurs at one point where the zenith angles of sun and sensor are identical and their azimuth angles are opposite. However, the ocean surface is never absolutely flat. The wind-derived surface roughness enlarges the sun glint area (see Figure 8).

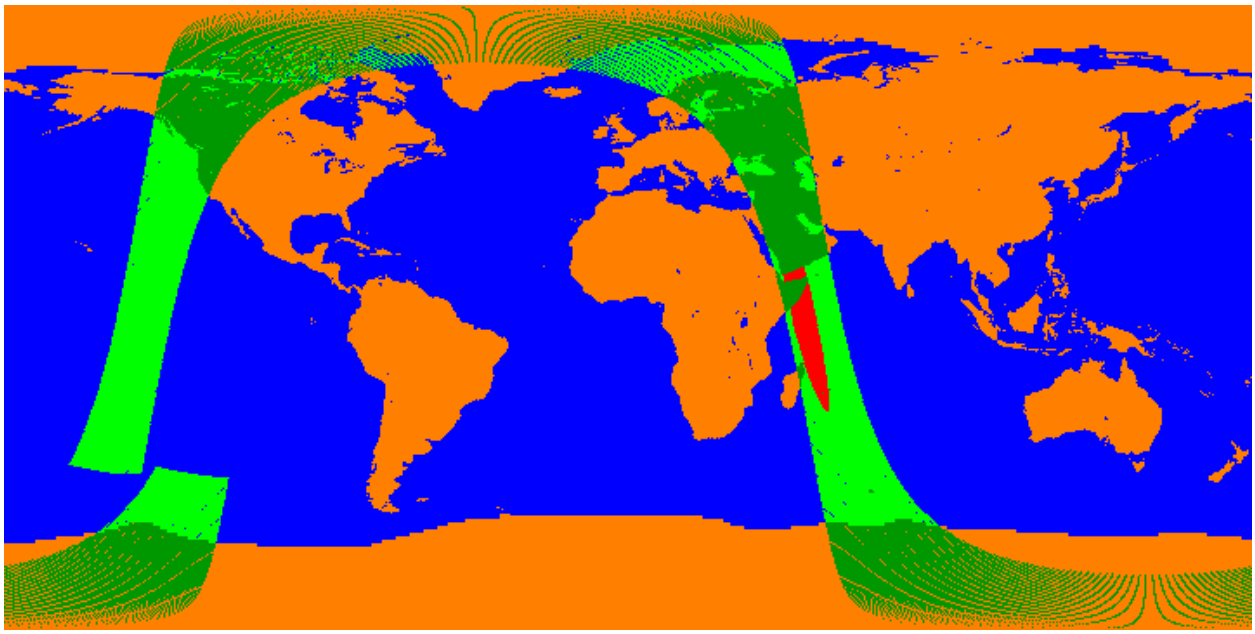

Figure 8. Sun glint (red color) area for a wind speed of 8 m s^{-1} for simulated 1330 VIIRS orbit.

In this document, we adopt the method from McClain and Yeh (1994) to determine when sun glint needs to masked out. The probability of a pixel being contaminated by sun glitter for the incoming sun direction (θ_0, ϕ_0) and the observing direction (θ, ϕ) can be written as

$$P = \frac{1}{\pi\sigma^2} \exp[-\frac{2(1+\cos\theta\cos\theta_0 + \sin\theta\sin\theta_0 \cos(\phi-\phi_0)) - (\cos\theta+\cos\theta_0)^2}{\sigma^2(\cos\theta+\cos\theta_0)^2}] \tag{7a}$$

where σ^2 is the mean square surface slope (Cox and Munk, 1954) which is a function of wind speed W_s

$$\sigma^2 = 0.003 + 0.00512\, W_S \tag{7b}$$

Figure 9 shows the distribution of the probability of a pixel contaminated by sun glitter. We use a threshold value of 1.5 percent for the probability to mask out the sun glint area. A correction is applied when the area is slightly contaminated by the sun glint.

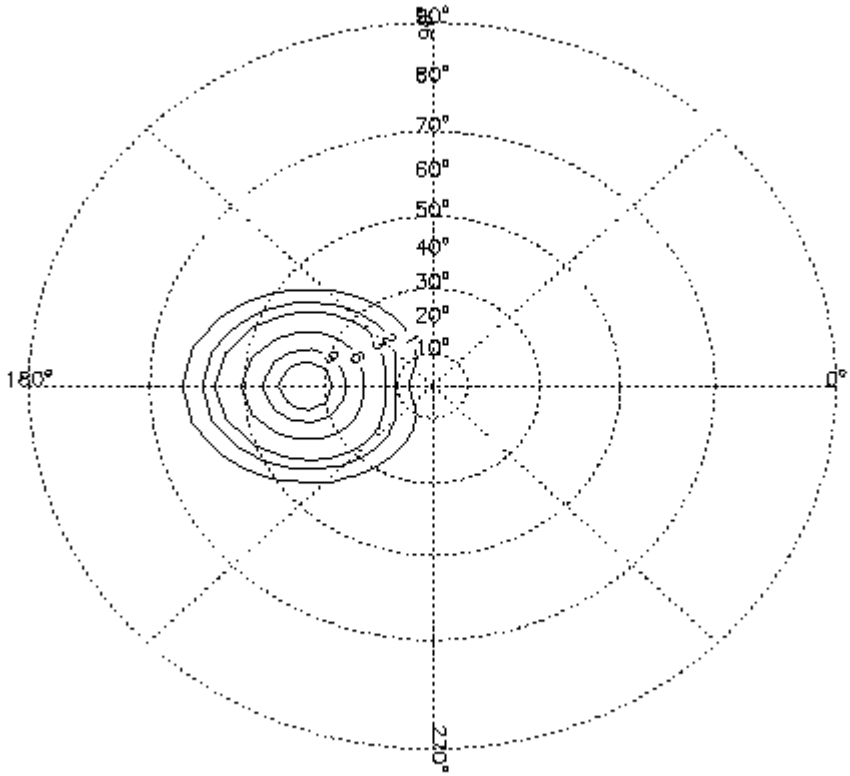

Figure 9. Sun glint probability contours (solid) for a sea surface wind speed of 5 m s^{-1} and sun zenith of 30°.

3.3.6 Algorithm Output

Outputs of the algorithm to be used for EDR processing are the remote-sensing reflectance R_{rs} in the VIIRS 412, 445, 488, 555, and 672 nm bands, the aerosol optical depth at 865 nm, and ε(751,865), the 751 nm/865 nm band ratio of single scattering aerosol reflectance. Quality indices or flags, such as for negative water-leaving remote sensing reflectance, absorbing aerosol, shallow water and turbid water, will also be produced.

3.3.7 Variance and Uncertainty Estimates

Variance and uncertainty estimates for retrieved water-leaving reflectances were presented by Gordon (1997a) for different sources of error. Below we briefly review error estimates for these sources of uncertainty.

Multiple scattering effects may be significant at the level of accuracy required for VIIRS. Although the single scattering approach works well for sufficiently small optical thickness, typically the case over the open ocean, it is desirable to consider extreme situations. The influence of multiple scattering depends significantly on the aerosol model. For example, for the maritime aerosol model, multiple scattering increases atmospheric reflectance by about 40 percent in comparison to single scattering. Multiple scattering effects are accounted for using look-up tables for twelve candidate aerosol models. Testing shows that the multiple-scattering algorithm retrieves water-leaving reflectance at 445 nm with uncertainty less than 0.002 for non-absorbing aerosol models.

The impact of aerosol absorption on multiple scattering may be strong. To account for the aerosol absorption effect, it is important that the relationship between particle size and absorption is approximately correct for each of the candidate aerosol models. Such a relationship must be based on climatology, e.g., when the aerosol optical thickness over the North Atlantic Saharan dust zone is high, we will use candidate models consisting of a linear combination of a maritime model and Saharan dust model.

Whitecaps have the potential of producing errors of a magnitude similar to the magnitude of the acceptable error. Measurements have shown that whitecaps may reflect considerably less in the near-infrared (NIR) than in the visible, presumably because a significant component of the whitecap reflectivity is due to scattering from submerged bubbles. The possible spectral dependence of the whitecap reflectivity is directly transposed onto the water-leaving reflectance spectrum, thus resulting in errors in chlorophyll concentrations derived from band ratio algorithms. If the error in the estimate of whitecap reflectivity at 445 nm is ±0.002, the error in the normalized water-leaving reflectance may range from approximately +0.0015, to -0.0025.

Aerosol vertical structure may affect the multiple scattering. Studies of this effect have shown that as long as the aerosol is weakly absorbing (ω_a>0.93), the error is negligible, but as ω_a decreases, the error becomes progressively larger. For example, the algorithm can tolerate only a ± 1 km error in the aerosol layer thickness for lookup tables calculated for the urban candidate model with physical thickness of 2 km.

In calculations of lookup tables for aerosol multiple scattering, polarization effects were considered (Liu and Ruprecht, 1996). Preliminary computation of polarization effects showed that possible uncertainty in water-leaving reflectance at 445 nm was acceptable, i.e., typically less than 0.001. Thus, compared to the errors possible when strongly absorbing aerosols or whitecaps are present, this error appears negligible.

Simulation showed that ignoring the surface roughness in computation of the lookup tables relating multiple scattering to single scattering reflectance values does not appear to lead to significant error.

Different seawater reflectance models have different behavior (Vasilkov et al., 1997). The Morel (1988) model is used for case I water and the Tassan (1994) model is used for case II water here.

3.4 ALGORITHM SENSITIVITY STUDIES

3.4.1 Calibration Errors

The calibration accuracy requirement for the atmospheric correction is very high because the atmospheric correction extracts the small water-leaving reflectance from the large TOA reflectance. To achieve 10% accuracy at the green band, a calibration accuracy of 0.5% is required, where perfect atmospheric correction is assumed. Such a high accuracy for the onboard radiometric calibration is thought to be beyond the capabilities of current sensors. Therefore, vicarious calibration of the sensor for ocean color is required (See Section 3.6.3). In this study, a 1.5% spectrally correlated calibration was investigated. The 1.5% calibration error may result in a 10 – 15% error for the accuracy of the water-leaving radiance.

3.4.2 Instrument Noise

The threshold requirement for chlorophyll measurement precision was the greater of 20 percent or TBD mg m^{-3}, and the threshold measurement range is 0.05 to 50 mg m^{-3}. Our resultant specification on the chlorophyll precision requirement imposes the strongest radiometric noise requirements for the VIIRS visible wavelength bands. We have used simulations of TOA radiances over the ocean to assess the effects of sensor noise in the visible and near-infrared VIIRS bands on the precision of chlorophyll retrievals, for each of the different VIIRS sensor performance models developed by Hucks (1998). The effects of noise in the visible bands and in the near-infrared bands were considered independently. Chlorophyll retrieval algorithms use water-leaving reflectances in the visible bands, and sensor noise in the near-infrared bands affects chlorophyll accuracy because it introduces errors in the visible band reflectances that are retrieved from the atmospheric correction algorithm.

The following procedure was used for our sensitivity study. TOA radiances were simulated for viewing geometries characteristic of the NPOESS 1:30 PM orbit on March 21, and for chlorophyll concentrations of 0.1, 1, and 5 mg m^{-3}. The Morel (1988) reflectance model for Case 1 waters was used to simulate water-leaving reflectance, and the 6S radiative transfer package was used to perform forward transfer to the TOA. Sensor noise was added to the simulated TOA radiances for each input chlorophyll concentration and for each of the VIIRS sensor performance models. One hundred random samples of the Gaussian noise distribution were obtained for each band and for each viewing geometry in a grid of 7 sensor zenith angles by 16 latitudes, covering the viewing swath. This provided 100 different maps of noise-added simulated radiance in each band. The Gordon-Wang atmospheric correction algorithm and the Carder et al. (1997) chlorophyll algorithm were applied to retrieve 100 different chlorophyll maps, and chlorophyll precision at each position was calculated as the standard deviation of the 100 chlorophyll values divided by the mean chlorophyll value. Thus, for each input value of chlorophyll concentration and each sensor performance model, maps of chlorophyll precision and mean retrieved chlorophyll concentration were obtained. Separate maps were also obtained of chlorophyll precision due to sensor noise in the visible bands and chlorophyll precision due to sensor noise in the NIR bands.

The full results of the sensitivity study are reported in reference *[V-1]* (see Section 1.3). The result of interest here is that, for a given sensor performance model, noise in the near-infrared bands has a much smaller effect on chlorophyll precision than noise in the visible bands. This is

shown in Figures 10 and 11. The reason is that, for a given measurement of TOA radiances, errors in the near-infrared bands lead to errors of the same sign in retrieved water-leaving reflectances in the visible bands. (The atmospheric correction algorithm fits a model aerosol spectrum to the near-infrared bands, and the near-infrared errors cause the model fit to be either systematically high or systematically low in the visible bands.) The chlorophyll retrieval algorithm makes use of ratios of water-leaving reflectances in different visible bands rather than absolute values of the reflectances, and these ratios are less affected by sensor noise in the near-infrared bands than the absolute values of reflectance are.

One of the NIR bands was located at 765 nm with a bandwidth of 40 nm. The final position of the NIR band is now at 751 nm with a bandwidth of 15 nm. The effects of sensor noise on chlorophyll precision had also been investigated for the case where a 10 nm wide band centered at 748 nm is used in place of the 40 nm wide band centered at 765 nm. This is intended to avoid the O_2 absorption feature at 762 nm. The narrower bandwidth results in greater sensor noise for a given VIIRS sensor performance model, but chlorophyll precision due to sensor noise gets only slightly worse. This is because sensor noise in the near-infrared bands still has a smaller effect on chlorophyll precision than sensor noise in the visible bands. Figure 12 shows a comparison of precision due to sensor noise for the different pairs of near-infrared bands, for the case of input chlorophyll concentration equal to 1.0 mg m^{-3}.

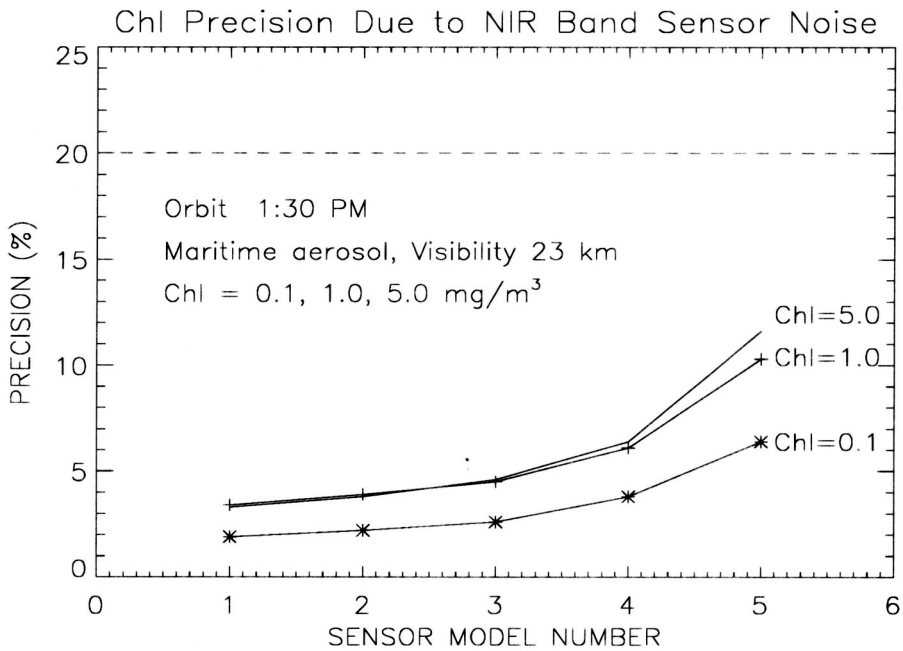

Figure 10. Mean chlorophyll precision due to sensor noise in the VIIRS near-IR bands as a function of VIIRS sensor performance model number. The precision values are averages for a 2400 km wide swath and solar zenith angle less than 70 degrees. The dashed line indicates the threshold requirement of 20 percent. The numbers on the x- axis represent models with worsening signal to noise ratio as the sensor model number increases. The Raytheon VIIRS final sensor noise level is between that given by sensor models 2 and 3.

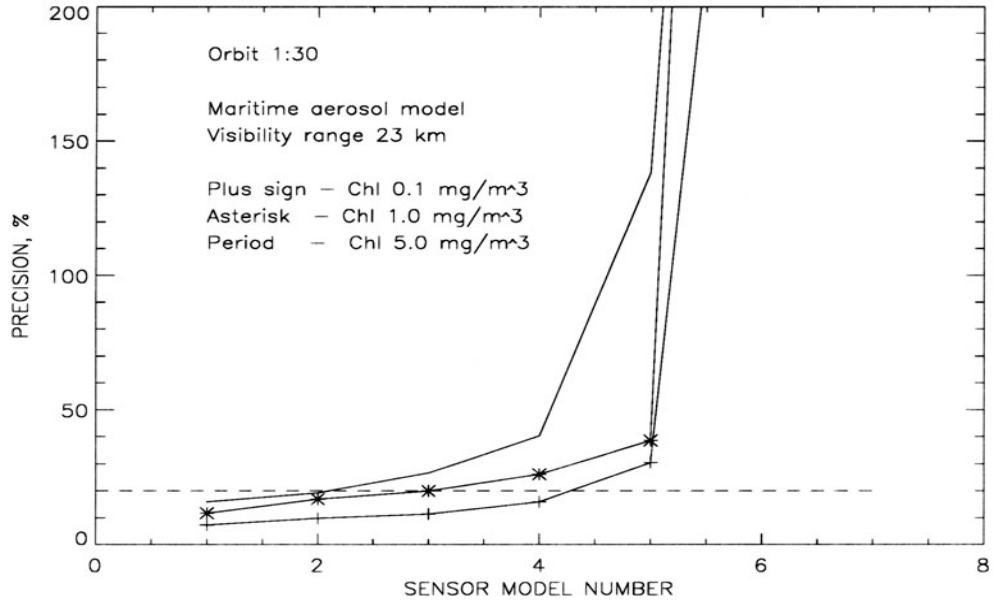

Figure 11. Mean chlorophyll precision due to sensor noise in the VIIRS visible bands as a function of VIIRS sensor performance model number. The precision values are averages for a 2400 km wide swath and solar zenith angle less than 70 degrees. The dashed line indicates the threshold requirement of 20 percent. The numbers on the x- axis represent models with worsening signal to noise ratio as the sensor model number increases. The Raytheon VIIRS final sensor is between that given by sensor models 2 and 3.

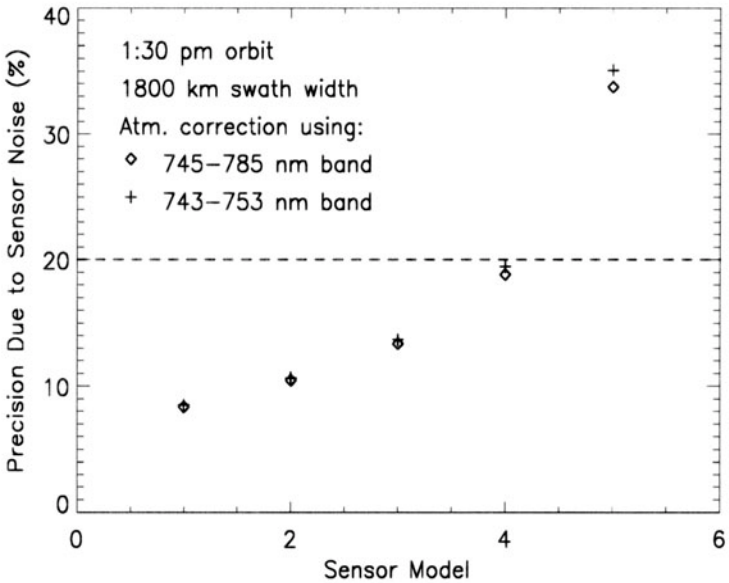

Figure 12. Chlorophyll precision due to sensor noise, averaged over the viewing swath of the 1:30 PM orbit, as a function of VIIRS sensor performance model. The results for atmospheric correction using the 745-785 nm and 841-876 nm band pair are shown as diamonds. The results using the 743-753 nm and 841-876 nm band pair are shown as crosses.

3.4.3 Stray light effect

Stray light contamination of the top-of-atmosphere (TOA) reflectances for cloud-free pixels that are close to cloud, deserts, or vegetated areas may affect ocean color retrievals (chlorophyll and suspended particulate matter concentrations). Semi-infinite non-ocean areas adjacent to the ocean are considered. The semi-infinite case is believed to be the worst. A 20 km by 20 km cloud is also considered. A source of the stray light is assumed to be the instrumental scattered light. TOA radiances over the ocean were simulated in the VIIRS bands. Stray light errors simulated for different sensor optics models were added to the TOA radiances. Gaussian radiometric noise was also added to the simulated TOA radiances. To isolate chlorophyll errors due to the stray light contamination, a perfect atmospheric correction (simply the subtraction of the atmospheric path radiance from the TOA radiance) was applied to the TOA radiance. The Gordon-Wang atmospheric correction algorithm was also applied to the TOA radiance (Gordon and Wang, 1994). Chlorophyll was retrieved from the water-leaving radiance by using both the Carder bio-optical algorithm (Carder et al., 1997) and the standard SeaWiFS algorithm, OC2v (O'Reilly et al., 1998). Accuracy and precision were calculated as a function of a distance from the cloud edge.

Top of atmosphere radiances over the ocean were simulated at 413, 443, 488, 555, 770, and 865 nm by using the 6S algorithm. This code uses the Morel reflectance model for Case 1 waters (Morel, 1988) to simulate water-leaving radiance for a given chlorophyll concentration and performs a forward transfer to the top of the atmosphere. The simulations were done for chlorophyll concentrations of 0.1, 1.0, and 5.0 mg/m^3 and the following standard atmospheric parameters: water vapor content of 0.85 g/cm^2, ozone content of 0.395 cm atm, maritime aerosol type, visibility of 23 km, and wind speed of 5 m/s. Geometric conditions correspond to the solar zenith angle of 40^0, and viewing zenith angles of 0^0 and 45^0, i.e. at the nadir and at the edge of a 1700 km swath. The pixel size was 1.3 km by 1.3 km.

The Morel (1988) reflectance model was chosen after comparing the predictions of three reflectance models with ship-based measurements from the SeaBAM dataset, which is described in the Ocean Color/Chlorophyll Flowdown Results document (Vasilkov and Odegard, 1998). The comparison showed that the Morel (1988) model provides the most realistic prediction of water-leaving reflectance at low chlorophyll concentrations.

Stray light error was added to the simulated TOA radiance for each pixel by using the results of calculations done by G. Godden and M. Wang (personal communication, 1999) for different optics models with two band positions (left side of FPA, and right side of FPA). The fore-optics and aft-optics PSFs are given by the following parameterization:

$$PSF_i = A_i 0.01^{-M_i} (633/\lambda_i) \left| sin(\theta_i + \varphi_i) - sin(\varphi_i) \right|^{M_i} (\alpha d_i)^2 \qquad (8a)$$

where λ is the wavelength and other parameters characterize a specific sensor optics model. Semi-infinite cloud formation (a long straight cloud edge) with a well-defined cloud edge was assumed. The calculations were done for the ratio of radiances over the cloud and the ocean $L_{cloud}/L_{ocean} = 20$. A cloud shadow effect was not considered. A horizontal cell size was assumed to be equal to 1.3 km. The stray light model for the 20 km by 20 km cloud was quite similar. The error was calculated along a line crossing the cloud center in a scan direction that was perpendicular to the cloud edge.

The stray light error was linearly scaled to the appropriate L_{cloud}/L_{ocean} values for the VIIRS visible and NIR bands. Cloud reflectance was assumed to be equal to 60%. The stray light error was introduced into the TOA radiance according to the following:

$$L(\lambda_i) = L_0(\lambda_i)\left[1 + \varepsilon_i \frac{R_{cloud}(\lambda_i)}{20 R_{ocean}(\lambda_i)}\right] \tag{8b}$$

where ε_i is the error in an *i*-th band calculated by the assumption that $L_{cloud}/L_{ocean} = 20$ and R is the TOA reflectance.

Sensor noise was added to the simulated TOA radiances for the baseline VIIRS sensor model 3 described by Hucks (1998). Noise equivalent delta radiance (NEdN) was calculated for a bandwidth of 20 nm at wavelengths 413, 443, 488, and 555 nm, which are used by the Carder algorithm. A random sample of the Gaussian noise distribution was obtained for each pixel. This provided about 300 different samples of noisy TOA and water-leaving radiances.

The retrieval of the chlorophyll concentration from the top-of-atmosphere radiances is performed in two steps: the atmospheric correction is performed to obtain remote sensing reflectance, and then a bio-optical algorithm is used to retrieve the chlorophyll concentration from the remote sensing reflectance. Two cases of the atmospheric correction were considered. To isolate chlorophyll errors due to the stray light contamination, a perfect atmospheric correction was first applied to the TOA radiance. The perfect atmospheric correction means that the atmospheric path radiance was simply subtracted from the simulated noise-added radiances. The Gordon-Wang atmospheric correction was also applied to the TOA radiance.

Chlorophyll precision was calculated as the standard deviation of the retrieved values divided by the mean chlorophyll value. Chlorophyll accuracy was calculated through the following relationship: (*mean – error_free)/error_free*, where *mean* is the mean retrieved chlorophyll and *error_free* is the retrieved chlorophyll value for the case where stray light error and sensor noise are not added to the simulated data. This definition of the chlorophyll accuracy based on the *error_free* value was used to avoid error due to the atmospheric correction itself and inconsistency between forward modeling of the TOA radiance and the Gordon-Wang atmospheric correction algorithm. The chlorophyll precision characterizes the effects of radiometric noise, and the chlorophyll accuracy characterizes the effects of stray light contamination.

A comparison of chlorophyll accuracy for the best and worst optics models is shown in Figure 13 for the case of a semi-infinite cloud with 60% reflectance. The solar zenith angle is 40^0, the observation is at nadir, and the true chlorophyll concentration is 0.1 mg/m^3. The chlorophyll accuracy is determined relative to the retrieved no-error chlorophyll value. No atmospheric correction removing stray light effects was applied. As it can be seen from Figure 13, the chlorophyll accuracy of 10% allocated for the stray light error source cannot be met within a 4 km area (or 3 pixels) adjacent to the cloud edge for the best model, model 2. For the worst model, model 4, about 12 pixels (16 km) adjacent to the cloud edge should be abandoned because the chlorophyll accuracy exceeds 10%.

It is interesting to note that the chlorophyll accuracy depends on the true chlorophyll concentration. Stray light effects are strongest for blue seawater, i.e. for low chlorophyll concentration. For no atmospheric correction removing stray light effects, stray light is simply

added to the water-leaving radiance. If we approximate the spectral ratio of the cloud TOA reflectance to the ocean TOA reflectance to a power law function: $R_{cloud}/R_{ocean} \sim (\lambda/\lambda_0)^n$, the remote-sensing reflectance of seawater will be $R_{rs}(\lambda) + r_0 (\lambda/\lambda_0)^{n-1}$. Most bio-optical algorithms make use of band ratios, i.e. $R_{rs}(\lambda_i)/R_{rs}(\lambda_k)$. The simplest algorithm, OC2, uses a single ratio $R_{rs}(490)/R_{rs}(555)$. The more sophisticated Carder algorithm uses three band ratios as well as the absolute value of remote sensing reflectance at 555 nm. It is obvious that stray light contamination will not affect chlorophyll retrievals of band-ratio algorithms if the spectral behavior of the remote sensing reflectance, $R_{rs}(\lambda)$, obeys the power law function $(\lambda/\lambda_0)^{n-1}$. The spectral behavior of the remote sensing reflectance, $R_{rs}(\lambda)$, is determined by the chlorophyll concentration. Thus, one can expect that for some range of chlorophyll concentrations the stray light effects would be minimal.

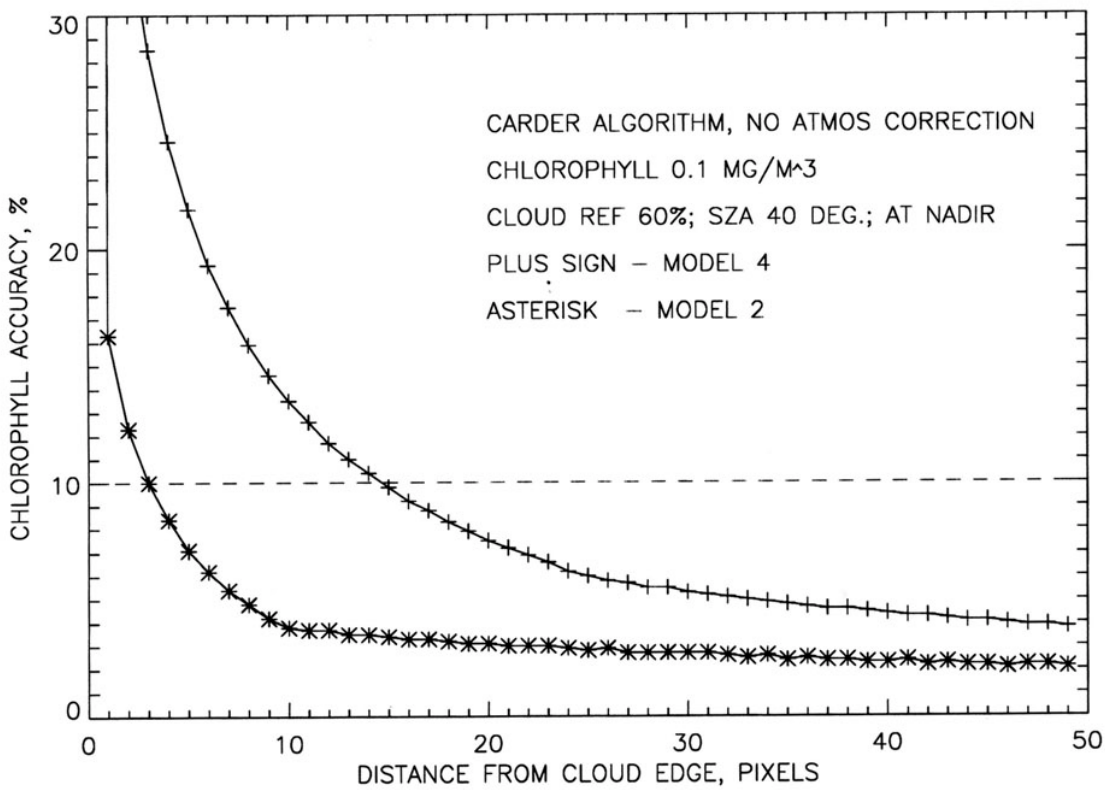

Figure 13. Chlorophyll accuracy as a function of a distance from the edge of a semi-infinite cloud. A dashed line represents the accuracy of 10% allocated for the stray light error source.

A comparison of the chlorophyll accuracy for the OC2 and Carder algorithms showed that the performance of the Carder algorithm is somewhat better than the OC2 algorithm performance.

Calculations done for the viewing zenith angle of 40^0 showed that the chlorophyll accuracy due to stray light contamination is slightly worse than for nadir observation at the same distance from the cloud edge.

Using the Gordon-Wang atmospheric correction algorithm dramatically changes the results described above. The atmospheric correction effectively removes the stray light contamination from the TOA radiances. A comparison of the chlorophyll accuracy for the cases of no atmospheric correction removing the stray light contamination and the Gordon-Wang atmospheric correction is shown in Figure 14. It can be seen that the stray light effects on the chlorophyll retrievals have practically been removed except for one pixel adjacent to the cloud edge. The chlorophyll accuracy due to stray light contamination is better than 3% except the pixel adjacent to the cloud edge. It has been mentioned that the spectral stray light contamination can be approximated by the power law: $(\lambda/\lambda_0)^{n-1}$. The atmospheric correction effectively interprets this contamination as a virtual aerosol contribution to the TOA radiance.

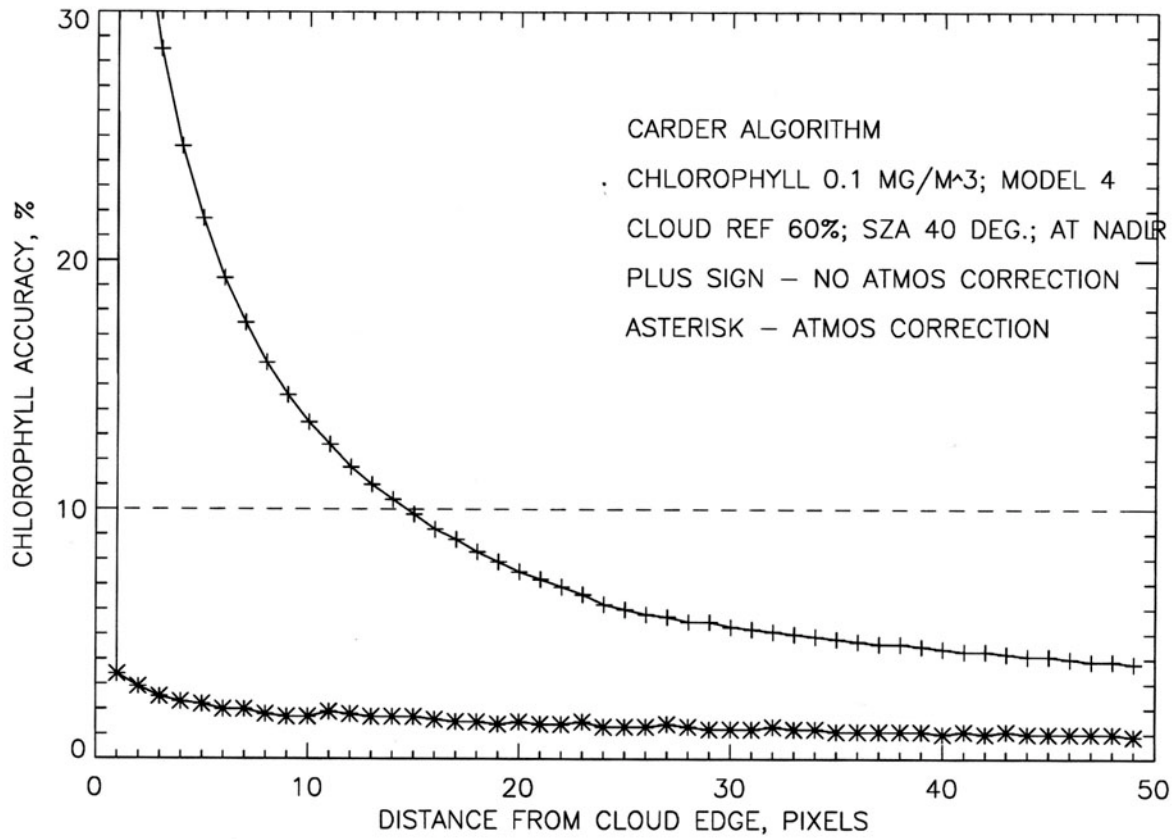

Figure 14. Comparison of the chlorophyll accuracy obtained with no atmospheric correction and the Gordon-Wang atmospheric correction algorithm. A dashed line represents the accuracy of 10% allocated for the stray light error source.

Semi-infinite desert and green vegetation areas adjacent to the ocean were also considered. It should be noted that for the case of green vegetation the true atmospheric correction was absolutely necessary to estimate stray light effects on chlorophyll retrievals. This is explained by the fact that the vegetation reflectance is low in the visible bands and very high in the NIR

bands. A comparison of the chlorophyll accuracy for cases of white cloud, sand, and green vegetation is shown in Figure 15. The stray light contamination caused by green vegetation affects the chlorophyll accuracy the most. The chlorophyll accuracy is worse than the 10% allocated for the stray light error source within at least three pixels (about 4 km) adjacent to the border between the ocean and terrain considered.

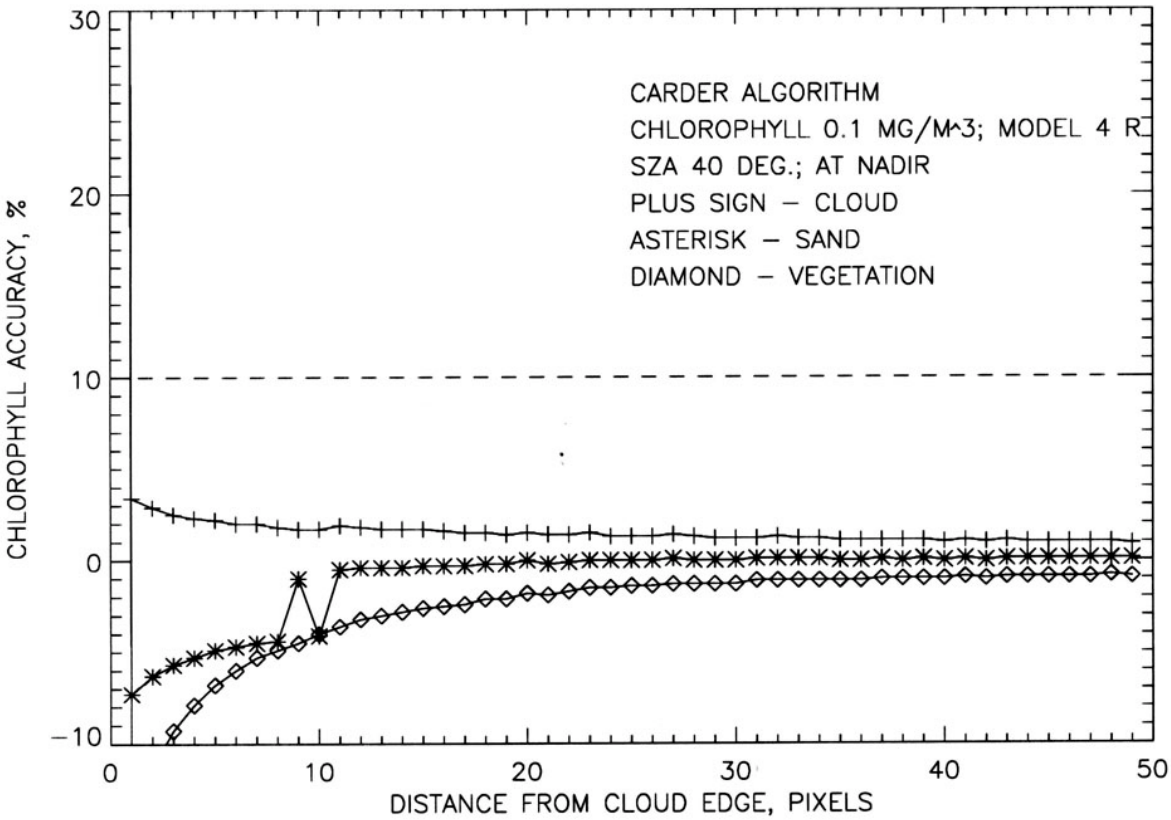

Figure 15. Comparison of the chlorophyll accuracy calculated for a semi-infinite cloud, desert, and vegetation. The Gordon-Wang atmospheric correction algorithm was applied to the TOA radiances.

The chlorophyll accuracy was also compared for the limited and semi-infinite clouds for the case of the Gordon-Wang atmospheric correction algorithm applied to the TOA radiances. The comparison is shown in Figure 16. The atmospheric correction effectively removes stray light effects for both the semi-infinite cloud and the limited cloud except for a couple of pixels adjacent to the cloud edge. The chlorophyll accuracy is slightly worse in the case of the semi-infinite cloud.

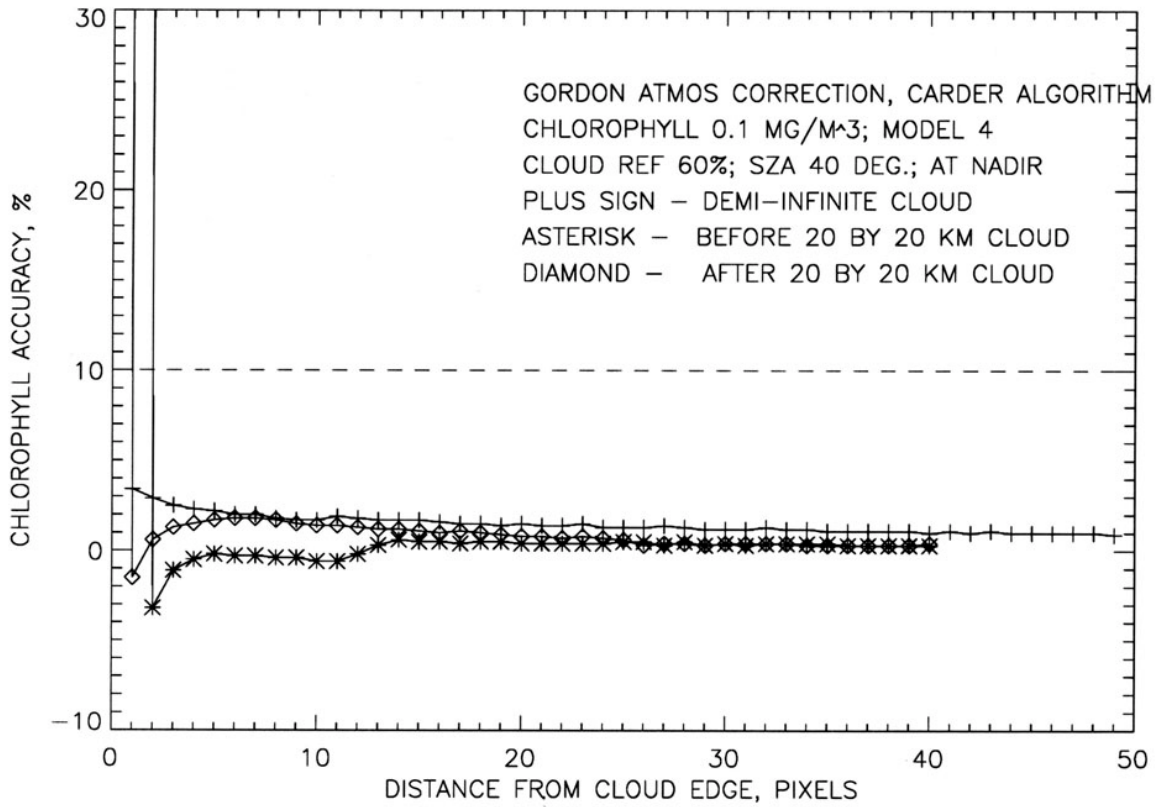

Figure 16. Comparison of the chlorophyll accuracy calculated for the semi-infinite and limited clouds using the Gordon-Wang atmospheric correction.

The atmospheric correction algorithm is able to effectively remove the stray light effects in which the spectral behavior is similar to the spectral contribution of aerosol to the TOA radiance. In the case of the effective removal of stray light contamination only one pixel adjacent to the cloud edge should be abandoned because it does not meet the chlorophyll accuracy of 10% allocated for the stray light error source. The stray light contamination due to a semi-infinite vegetated area adjacent to the ocean has a greater affect on the chlorophyll retrievals than a semi-infinite cloud does. The chlorophyll accuracy is worse than 10% within three pixels (about 4 km) adjacent to the border between the ocean and vegetated area.

3.4.4 Residual instrumental polarization

The quality of bio-optical products from satellite ocean color sensors is strongly dependent on the accuracy of sensor measurements of the top-of-the-atmosphere (TOA) radiance. Radiation measured at the top of the atmosphere is generally polarized. Because all color sensors have some polarization sensitivity, the radiance measured by the sensor will be biased. This error in the TOA radiance due to the instrumental polarization sensitivity can affect the accuracy of the final bio-optical product of the ocean color sensors. It is of practical interest to estimate how well atmospheric correction and bio-optical algorithms can tolerate significant instrumental polarization. The performance of bio-optical algorithms may vary for polarization-induced errors depending on the particular algorithm. The acceptable magnitude of the sensor polarization

sensitivity should be determined from the bio-optical product error allocated for polarization-induced error source.

Basically, there are two options for estimating the acceptable magnitude of the sensor polarization sensitivity. If the polarization state of the TOA radiation is not accounted for by an atmospheric correction algorithm, the requirement for the sensor polarization sensitivity should be the acceptable maximum. However, if the atmospheric correction algorithm allows correction for the polarization-induced error, requirements for the sensor polarization sensitivity should be formulated. This characterization should include both the amplitude and phase angle of the sensor polarization sensitivity.

The sensor-measured Stokes vector $\mathbf{I_m}$ can be represented by:

$$\mathbf{I_m} = \mathbf{M}\ \mathbf{R}(\alpha)\ \mathbf{I}_t \tag{9}$$

where $\mathbf{I_t}$ ={*I, Q, U, V*} is the TOA Stokes Vector, $\mathbf{R}(\alpha)$ is the rotation matrix transferring $\mathbf{I_t}$ from the calculation-based reference plane, which contains the propagation direction of the light and the vertical axis, to the instrument-based reference plane, α is the angle between the two reference planes, and $\mathbf{M}$ is the instrument Mueller matrix, describing the sensor response to the input Stokes vector. The first element m_{11} of $\mathbf{M}$ can be taken as 1 by the calibration. The measured intensity I_m then is:

$$I_m = I_t + m_{12}(Q_t \cos 2\alpha + U_t \sin 2\alpha) + m_{13}(-Q_t \sin 2\alpha + U_t \cos 2\alpha) \tag{10}$$

where we neglect the component V_t. By introducing the degree of the polarization, *P*, of the TOA light

$$\frac{Q_t}{I_t} = P\cos 2\varphi\,, \quad \frac{U_t}{I_t} = P\sin 2\varphi\,,$$

and using the instrument polarization sensitivity, P_{in}, and polarization phase angle, χ_{in},

$$m_{12} = P_{in}\cos 2\chi_{in}\,, \quad m_{13} = P_{in}\sin 2\chi_{in}$$

we can rewrite (2) in the following form:

$$I_m = I_t[1 + P_{in} P \cos 2(\alpha - \varphi - \chi_{in})] \tag{11}$$

The relative error of the measurement of intensity can be represented as:

$$\frac{\Delta I_t}{I_t} \equiv \frac{I_m - I_t}{I_t} = PP_{in}\cos 2(\alpha - \varphi - \chi_{in}) \le PP_{in} \tag{12}$$

The instrumental polarization sensitivity is a measure of the sensor response to completely linear polarized light. It is defined as:

$$P_{in} = \frac{I_{\max} - I_{\min}}{I_{\max} + I_{\min}} \tag{13}$$

where $I_{\max}$ and $I_{\min}$ are the maximum and minimum of the measured radiance for linearly polarized source radiance for which the plane of polarization contains the line of sight and has any orientation about the line of sight. In practice, the instrumental polarization sensitivity is known with some error ΔP_{in} and the polarization phase angle is known with some error $\Delta\chi_{in}$.

The problem of the effects of the instrumental polarization sensitivity on bio-optical retrievals can be formulated as follows. Given the uncertainty in the bio-optical product allocated for polarization-induced error, one should derive the requirements for the instrumental polarization sensitivity and phase angle assuming at least the two following cases: The first case is an atmospheric correction algorithm not accounting for the polarization state of TOA radiation. The requirement for this case should set up an acceptable maximum for the sensor polarization sensitivity, P_{in}. The uncertainties in the sensor polarization sensitivity and phase angle do not play a role. The second case is an atmospheric correction algorithm accounting for the polarization state of TOA radiation. The acceptable maximum for the sensor polarization sensitivity should be established in this case as well but this should be accompanied by requirements to sensor polarization characterization including the uncertainties in the sensor polarization sensitivity, ΔP_{in}, and phase angle, $\Delta\chi_{in}$. These requirements strongly depend on the manner of polarization correction introduced in the atmospheric correction algorithm. All of the above requirements should also be considered from the point of view of their technical feasibility because the polarization requirements may be contradictory to other sensor requirements. For example, using a polarization scrambler may not feasible for a specific sensor because of its deterioration of sensor stray light characteristics.

The degree of linear polarization (P, a measure of the polarization of the atmosphere-Earth source system) for VIIRS is between 0 and 60% (25% is a typical value at 443 nm; see Figure 17). Linear polarization decreases with the increase of the aerosol optical thickness (Figure 18). For a given aerosol optical depth, the linear polarization depends slightly on aerosol type (Figure 19). The measurement error in radiance/reflectance results from the residual instrumental polarization depends on residual instrumental polarization sensitivity (P_{int}), polarization angle (c_{int}), and P of the radiation source.

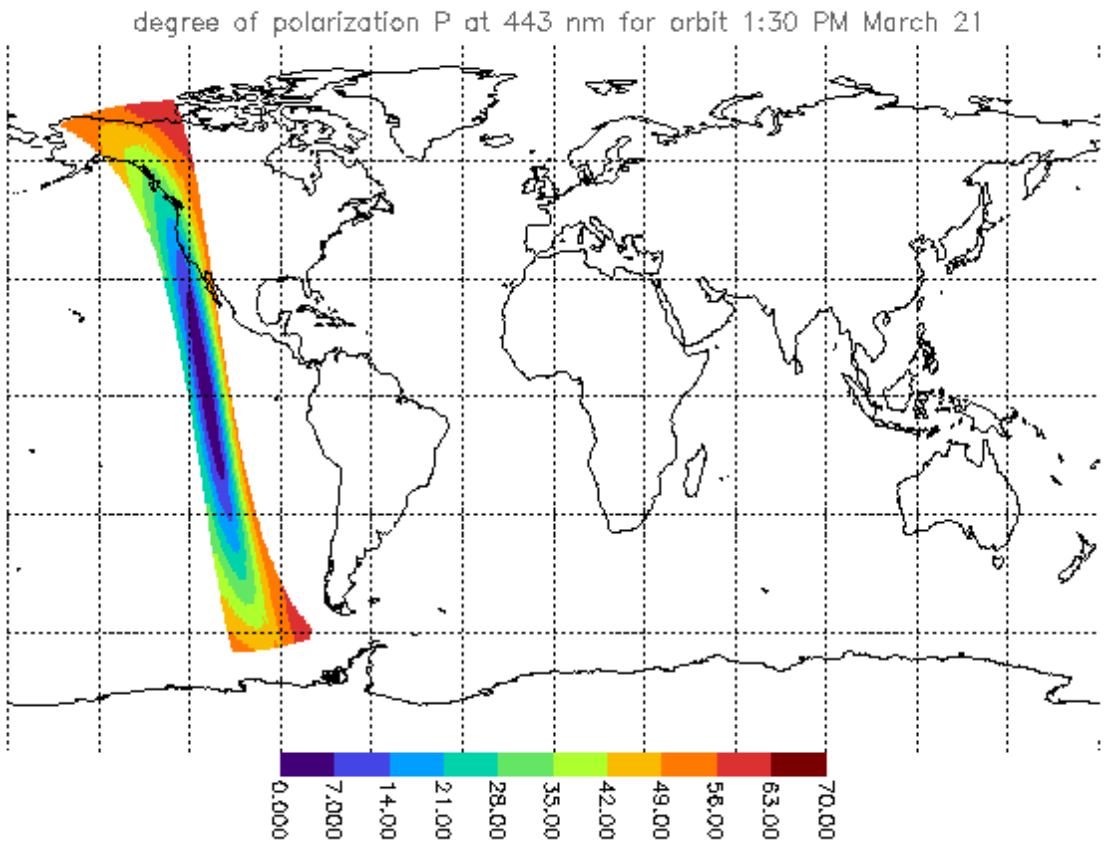

Figure 17. Degree of polarization at 443 nm.

$$\frac{\Delta I_t}{I_t} = 0.5 \times 0.03 = 0.015$$

For a stressing case (low sun and viewing angle of 47 degree) and a residual instrument polarization sensitivity of 2%, the relative error on radiance/reflectance at blue bands from Eq.(12) is approximately 1.5%. The 1.5% error in TOA radiance can result in a 15% error for the remote sensing reflectance. A correction is required for 3% residual instrumental polarization for the stressing case.

The linear polarization P changes with the aerosol optical thickness (see Figure 18).

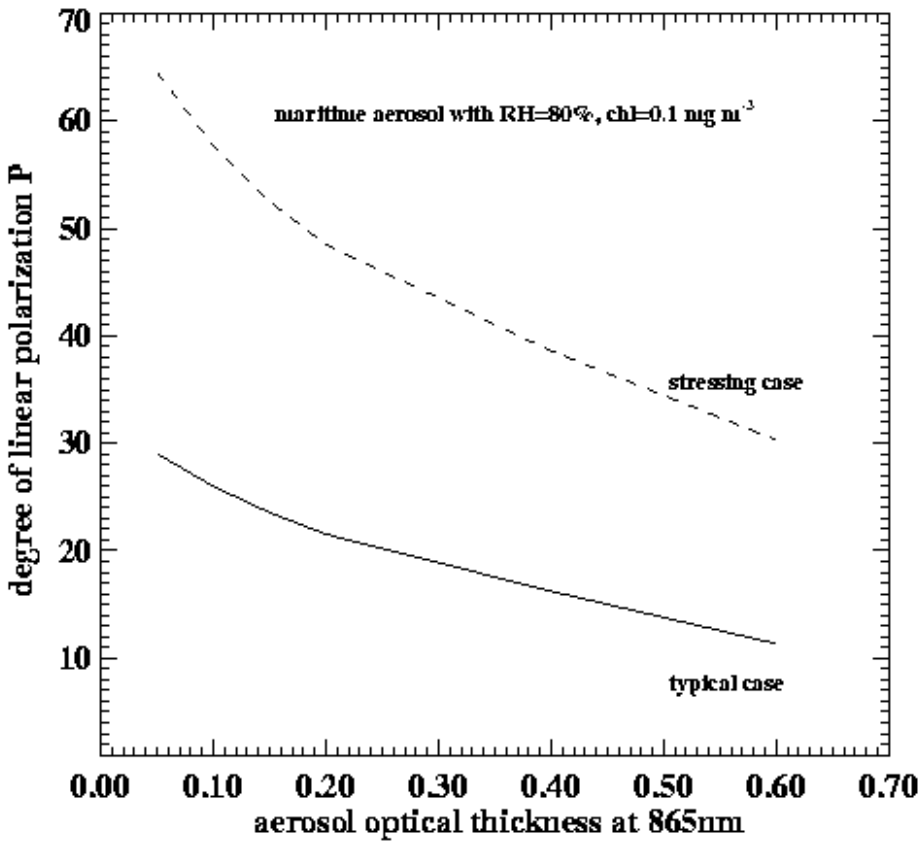

Figure 18. Variation of linear polarization with the optical depth of the aerosol.

For a given aerosol optical thickness of 0.15,variation of linear polarization P at 413 nm is within 0.05.

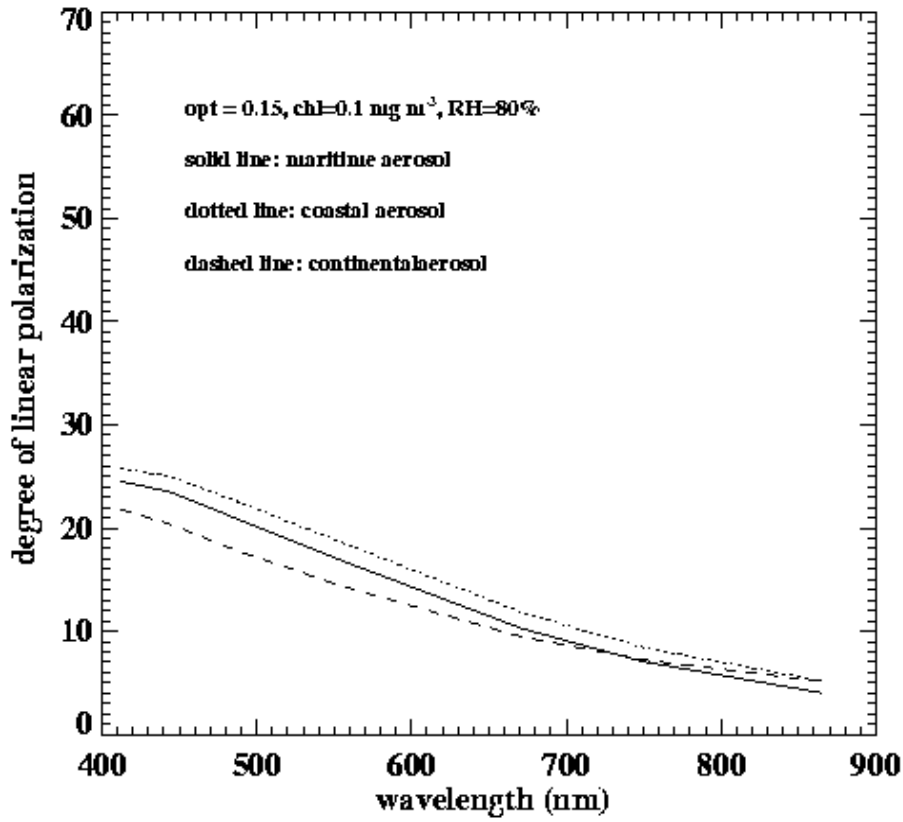

Figure 19. Sun zenith = 41 degree, viewing = 30 degree, Relative azimuth = 90 degree, chlorophyll = 0.1 mg/m3

Gordon et al. (1997b) have studied the effect of the residual instrumental polarization on the water-leaving radiance. We have developed a two-step algorithm to reduce the effect of the residual polarization error. The algorithm uses the Gordon-Wang algorithm and look-up tables based on fully polarized code. Using optical thickness and aerosol type from the first step to correct residual polarization, the atmospheric correction algorithm is performed again. The two-step algorithm reduces the error of the chlorophyll concentration retrieval dramatically (Figure 20).

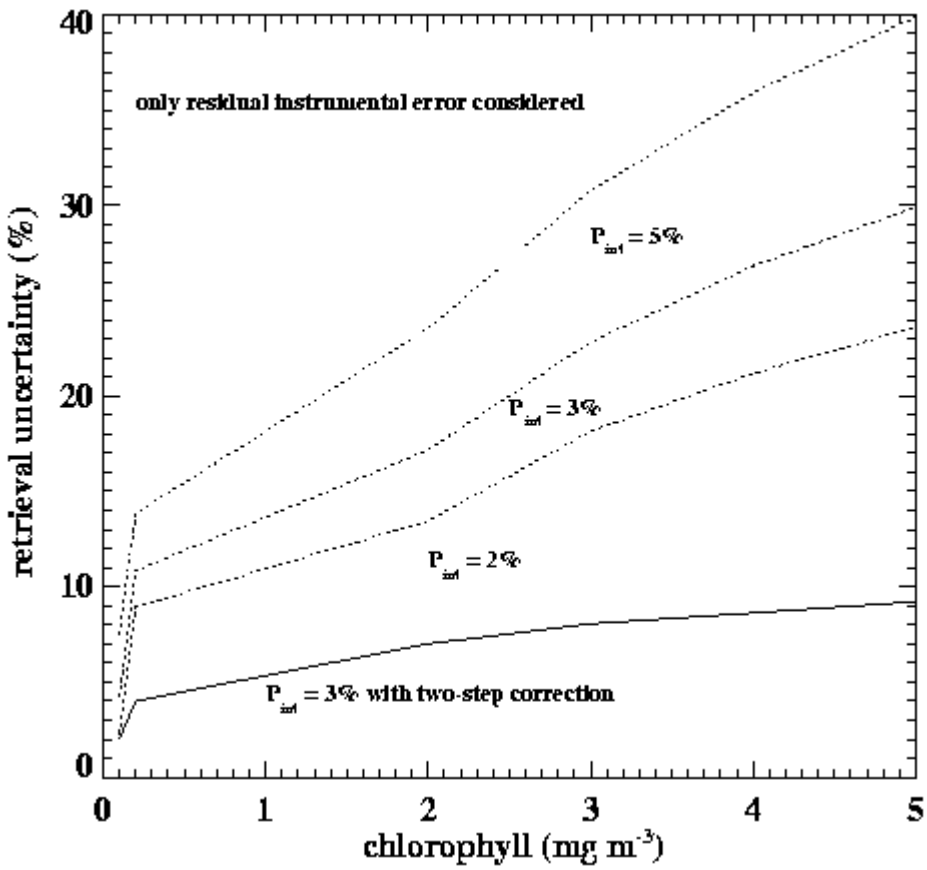

Figure 20. Retrieval uncertainty for various polarization sensitivities. The two-step algorithm yields the best results.

3.4.5 Absorbing aerosols

There are no chlorophyll retrievals in huge areas of the Atlantic Ocean from SeaWiFS. Those areas have been masked by SeaWiFS because the atmospheric correction algorithm resulted in negative water-leaving radiances. This atmospheric correction algorithm failure is caused by Saharan dust blown over the ocean by the westward winds. Maritime aerosol is non-absorptive because its single scattering albedo is about 1 at 555 nm. The single scattering albedo for desert dust aerosol is about 0.8 in the winter; therefore desert dust aerosol is absorbing aerosol. In addition, the epsilon value for non-absorbing and absorbing aerosols is quite different (see Figure 21). We have included desert, urban, and volcanic aerosols in the look-up table so that the algorithm can treat absorbing aerosols. However, the problem of absorbing aerosols is quite complex.

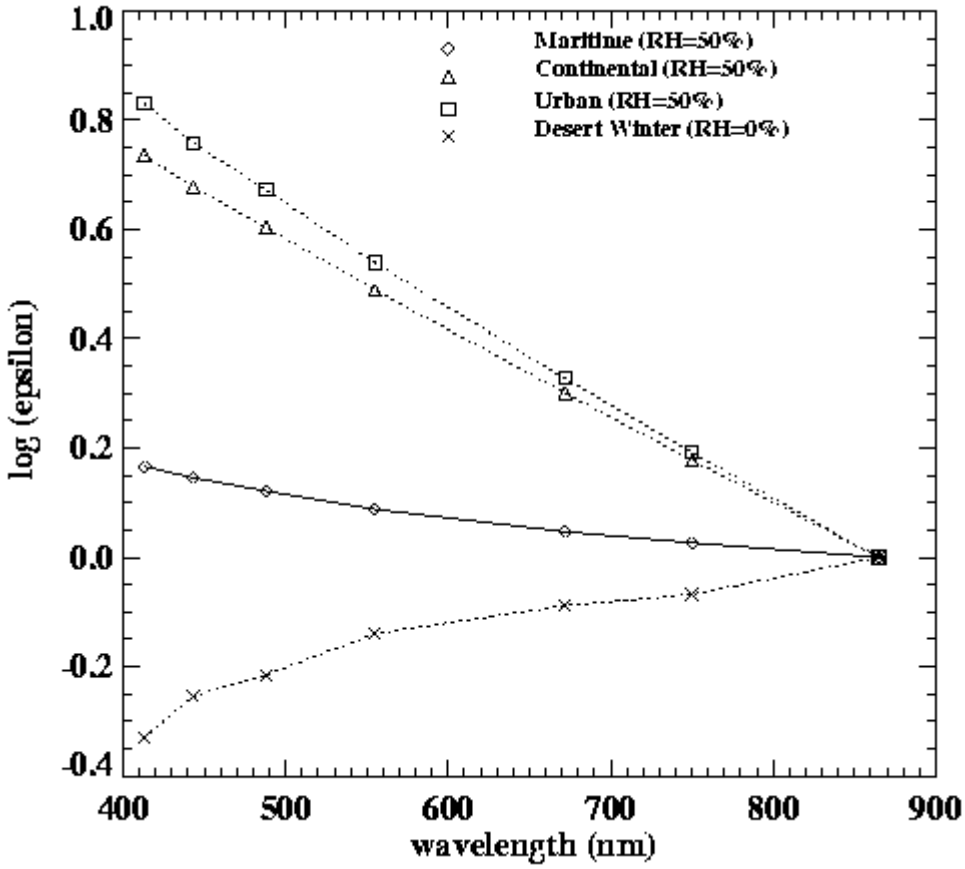

Figure 21. Variation of ε(λ, 865) for nadir viewing with a sun zenith angle of 41° for the maritime, continental and urban aerosol models for RH=50% and a desert aerosol (wintertime) with RH=0%.

3.5 PRACTICAL CONSIDERATIONS

3.5.1 Numerical Computation Considerations

Gordon (1996) has presented test results of the speed of computation for a preliminary implementation of the atmospheric correction algorithm for SeaWiFS. The speed in pixels processed per second of real time for a single processor of each of five computers is shown in Table 2. Further information on computation speed can be found in the VIIRS Computer Resource Requirements *[Y-3257]*.

3.5.2 Correction to the Instrumental Polarization

The specification value for the instrumental polarization sensitivity is 3% provided that two-step polarization correction algorithm is performed. The first step of the two-step algorithm is using a SeaWiFS/MODIS-like standard procedure to obtain the aerosol type and aerosol optical depth. In the second step, the input measurements are adjusted using the sensor and aerosol characteristics and the standard atmospheric correction is performed again. By the end of phase II,

RAYTHEON has achieved a much better design than the specification value for the polarization sensitivity (see chart 189, VIIRS Sensor Technical Interchange Meeting, November 27-29, 2001). The instrumental residual polarization sensitivity for NIR bands is as low as about 0.5%. This value implies that a SeaWiFS/MODIS like standard atmospheric correction algorithm can be used along with a polarization correction for the blue, green, and yellow bands. The polarization correction algorithm has been implemented.

Table 2. Processing Speeds for Preliminary Implementation of the Atmospheric Correction Algorithm for SeaWiFS

Computer	Frequency (MHz)	Processing Rate (pixels/s)
SGI 4D/480	40	181
SGI Indigo 2	150	509
DEC 3000/400	133	569
DEC 3000/500	176	679
DEC 7000/610	183	860

3.5.3 Stray Light Warning Flag

Scatter light is defined as light contamination from the instrument itself, for example the instrument surface roughness. Stray light is defined as the effect of inhomogeneous scenes, such as a scene composed of cloud and clear ocean surface. In practice, the scatter light and stray light cannot be strictly separated. In this section, we discuss the stray light flag only.

As shown in Figure 14, the chlorophyll accuracy of 10% allocated for the stray light error source can be met, except within a pixel of a cloud edge. In these circumstances, atmospheric correction processing will still be carried out, but the cloud adjacency flag from the VIIRS Cloud Mask will be passed along as a warning that stray light contamination from clouds is possible. Stray light contamination for pixels adjacent to land is also possible, but atmospheric correction will also be carried out in these cases as well. Pixels adjacent to land are likely to be flagged as coastal, shallow water, or turbid.

3.5.4 Programming and Procedural Considerations

Programming and procedural considerations here are similar to those of SeaDas. SeaDas is an operational system for SeaWiFS data. Besides the functions of SeaDas, the software developed here has taken account of absorbing aerosol, the correction to the residual instrumental polarization, and turbid and shallow waters.

3.5.5 Quality Assessment and Diagnostics

Flags are given to indicate the quality of the retrieval. Flags indicate valid data, negative water leaving reflectance, cloud contamination, turbid water, shallow water, and absorbing aerosol.

3.5.6 Exception Handling

Exceptions will occasionally prevent operation of the algorithm, such as missing VIIRS data or unavailable ancillary data. Errors in retrieved water-leaving reflectances can also cause exceptions in algorithms that use water-leaving reflectances as inputs. A set of flags is given to indicate situations when atmospheric correction should not be attempted, when the algorithm fails, or when the retrieved values are not realistic (e.g., negative values of water-leaving reflectance).

3.5.7 Masks and Flags

The Atmospheric Correction EDR product uses the same mask and flag information for data processing as the Ocean Color EDR. Please refer to [V-2] for descriptions of the masks and flags used.

3.6 ALGORITHM VALIDATION

3.6.1 Error Budget

Performing the following steps generated the error budget:

a) Utilizing a perfect sensor and perfect ancillary/auxiliary inputs.

b) Introducing error in the ancillary/auxiliary inputs.

c) Introducing the radiometric noise.

d) Introducing the calibration stability error.

e) Introducing residual instrumental polarization sensitivity.

The error due to stray light is estimated. The band-to-band registration error is small and negligible. The error due to “cloud masked where clear” does not affect the error budget. See the VIIRS Error Budget *[Y-3249]* document for further details of the error budget. According to this error budget document *[Y-3249]*, the performance (i.e. using predicted radiometric noise) for fine resolution is better than the specification value.

3.6.2 Global maps of remote sensing reflectance and retrieval of chlorophyll

The chlorophyll concentration was used as input for our forward radiative transfer model. Maritime aerosol with relative humidity of 80% and a visibility of 23 km is used. Sun glint was not considered in the calculation because the overlap of the 9:30 AM and 1:30 PM orbits can eliminate most parts of the area contaminated by sun glint. It can be seen from Figure 22 that low remote sensing reflectance occurs in areas with high chlorophyll concentration (see Figure 22). The retrieval algorithm for the chlorophyll concentration uses water-leaving remote sensing reflectance at 413, 445, 488, 555 nm. The chlorophyll retrieval uncertainties are given in Figure 23.

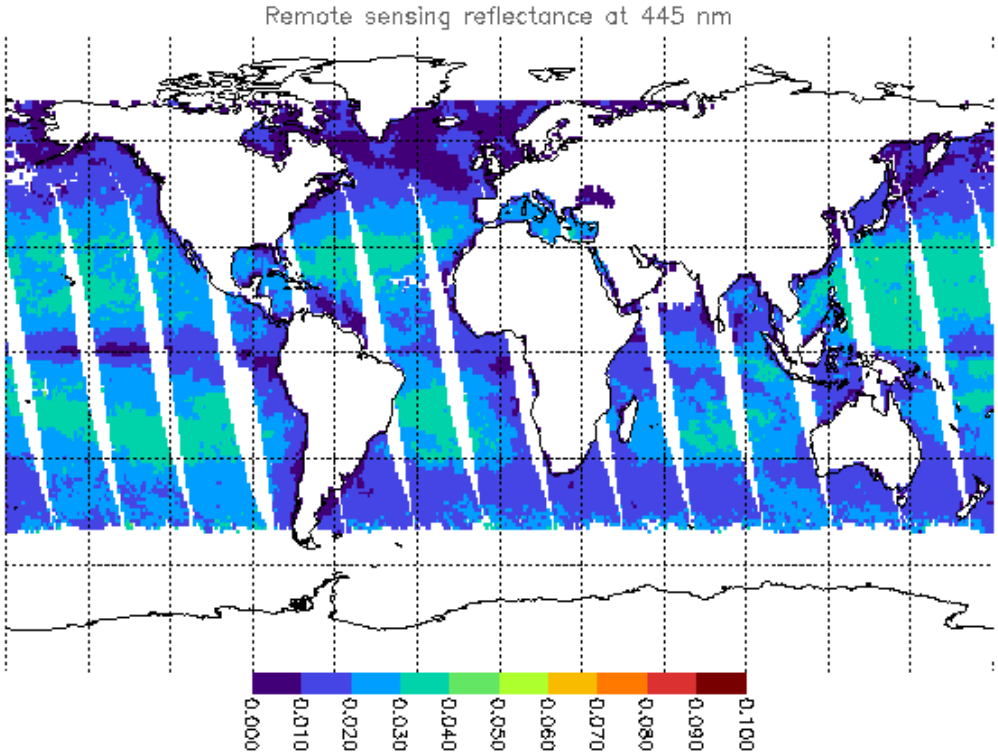

Figure 22. Retrieved remote sensing reflectance.

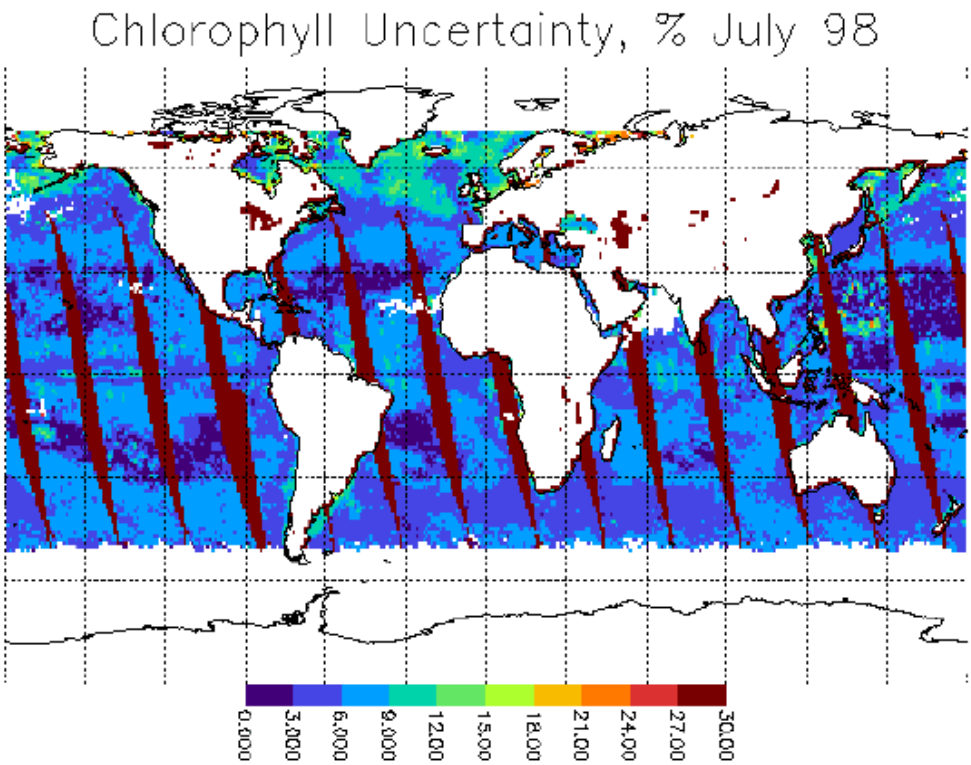

Figure 23.Uncertainty of the retrieval of the chlorophyll concentration.

3.6.3 Post-launch validation

Post-launch validation of retrieved water-leaving reflectances will make use of VIIRS solar and lunar measurements, and vicarious calibration using measurements made at the ocean surface from fixed moorings and ships. The validation approach for VIIRS incorporates methods developed for SeaWiFS and MODIS validation (McClain et al., 1992; Mueller and Austin, 1995; Clark et al., 1997). Measurements of an onboard calibration source and measurements of an onboard solar diffuser will be used to correct for any short-term variations in sensor stability in each wavelength band. Vicarious calibration will be performed after any such time-dependent corrections are applied to the VIIRS data.

Vicarious calibration will make use of measurements of water-leaving reflectance in the VIIRS 412, 443, 488, 555, and 645 nm bands from fixed buoys and ships at open ocean sites characterized by optically clear water and marine aerosols. These measurements will be made simultaneously with VIIRS retrievals of water-leaving reflectances for pixels containing the sites. Retrieved and *in situ* reflectance values will be compared to obtain a calibration gain correction factor for each wavelength band. Ratios of retrieved to *in situ* reflectance for each band will be examined for any trend with time or with atmospheric path length, to check for possible errors in the time-dependent calibration gain factors or possible deficiencies of the atmospheric correction algorithm. Temporal trends will also be identified in retrieved values of

normalized water-leaving reflectance for open ocean, clear water (retrieved chl a < 0.15 mg m^{-3}) pixels.

This vicarious calibration method cannot be applied to the VIIRS 765 and 859 nm bands because the atmospheric correction algorithm assumes water-leaving reflectance values are zero in these bands. The pre-launch calibration of the 859 nm band will be assumed to be correct, and a calibration gain correction factor for the 765 nm band will be determined assuming $\varepsilon(765,859) = 1.0$, which is typical of marine aerosols. (The quantity $\varepsilon(765,859)$ is the 765 nm/859 nm band ratio of single scattering aerosol reflectance.) This correction factor is determined by comparing the ratio of measured VIIRS radiances in the 765 and 859 nm bands, averaged over many measurements of the calibration sites, with the ratio predicted by a radiative transfer calculation for $\varepsilon(765,859) = 1.0$.

This method of vicarious calibration has been applied to SeaWiFS data using surface measurements from the marine optical buoy (MOBY) located off of Hawaii, and the calibration has been verified using ship-based measurements such as those from the Atlantic Meridional Transect Program (Robins et al., 1996). A similar vicarious calibration procedure is required for VIIRS data using surface measurements from MOBY and any other fixed open-ocean optical measurement moorings that may be operational in the NPOESS era. After application of vicarious calibration, retrieval of water-leaving reflectances will be validated for a wide range of geophysical conditions using surface measurements from NPOESS validation cruises that will take place shortly after the NPOESS launch, as well as from any cruises that may take place at roughly the same time for calibration and validation of other ocean color sensors.

Validation should be performed for conditions that are difficult for atmospheric correction, including the presence of urban aerosols, desert dust, stratospheric aerosols and/or thin cirrus clouds, turbid coastal waters, whitecaps, and broken cloud fields or islands (to examine the effect of stray light on atmospheric correction). Clark et al. (1997) have described plans for validation of MODIS atmospheric correction under these conditions. Surface measurements to be performed include measurement of water-leaving radiance in the direction of the sensor, chlorophyll concentration in the vicinity of the ship, spectral aerosol optical thickness and spectral sky radiance at angles close to and far from the solar zenith and azimuth angles, vertical aerosol distribution using lidar, and spectral whitecap reflectance. Results of validation studies for SeaWiFS, MODIS, and other pre-NPOESS ocean color sensors will be taken into account in development of a detailed validation plan for VIIRS.

3.7 ALGORITHM DEVELOPMENT ACTIVITIES (P^3I)

For turbid water, we may apply the algorithm developed by Hu et al. (1999, private communication). This algorithm applies the aerosol properties over less turbid water to the turbid water. For shallow water, we may use the same concept. These algorithms need to be extended for our operational scheme. For the absorbing aerosols, our algorithms can treat desert and volcanic aerosols, but work on these cases is not complete and needs to continue.

4.0 ASSUMPTIONS AND LIMITATIONS

4.1 ASSUMPTIONS

The Gordon-Wang algorithm makes use of the following assumptions:

(1) The aerosol models used are representative of aerosols present over the ocean.

(2) Water-leaving reflectance is zero in two near-infrared wavelength bands.

(3) The formulation of whitecap reflectance as a function of wind speed and electromagnetic wavelength is valid.

(4) The two-layer plane-parallel model atmosphere adopted for radiative transfer calculations is valid.

4.2 LIMITATIONS

The assumptions listed above are not always valid:

(1) The algorithm performs poorly in cases where strongly absorbing aerosols are present. Methods of modifying atmospheric correction algorithms to handle strongly absorbing aerosols are under investigation (e.g., Gordon, 1997).

(2) Water-leaving reflectance in the NIR bands is not negligible in turbid coastal waters or in coccolithophore blooms. Techniques are under investigation for atmospheric correction over turbid coastal waters, which determine the water-leaving reflectance at 765 nm using a simple model for the spectral dependence of water-leaving reflectance in the NIR (e.g., Ladner *et al.*, 1998; Stumpf *et al.*, 1998). It may also be possible to use aerosol properties derived for a nearby deep, non-turbid water pixel to perform the atmospheric correction over turbid coastal waters.

(3) Further studies of the dependence of whitecap reflectance and the magnitude of its contribution at the TOA on wind speed and wavelength should be made.

5.0 ACKNOWLEDGEMENTS

The authors of Version 5 of this ATBD would like to acknowledge Nils Odegard and Alexander Vasilkov, authors of the Version 4 ATBD, on which this version is based. We would also like to acknowledge a former Science Team Member, Menghua Wang of the University of Maryland Joint Center for Earth Systems Technology, who also made contributions to the development of previous versions of this ATBD.

6.0 REFERENCES

Carder, K., S. Hawes, and R.F. Chen (1997). Case 2 Chlorophyll_a Algorithm and Case 2 Absorption Coefficient Algorithm. MODIS ATBD 19.

Clark, D.K., H.R. Gordon, K.J. Voss, Y. Ge, W. Broenkow, and C. Trees (1997). Validation of atmospheric correction over ocean. *J. Geophys. Res*., 102, 17209.

Cox, C., and W. Munk (1954). Measurements of the roughness of the sea surface from photographs of the sun's glitter. *J. Opt. Soc. Amer*., 44, 838.

Frouin, R., M. Schwindling, and P.-Y. Deschamps (1996). Spectral reflectance of sea foam in the visible and near-infrared: In situ measurements and remote sensing implications *J. Geophys. Res*., 101, 14361.

Gordon, H.R. (1996). Normalized Water-leaving Radiance Algorithm Theoretical Basis Document. MODIS ATBD 17.

Gordon, H.R. (1997a). Atmospheric correction of ocean color imagery in the Earth Observing System era. *J. Geophys. Res*., 102, 17081.

Gordon, H. R., Tao Du, and Tianming Zhang (1997b), Atmospheric correction of ocean color sensors: analysis of the effects of residual instrument polarization sensitivity. *Appl. Opt*., Vol. 36, pp. 6938-6948.

Gordon, H.R., J.W. Brown, and R.H. Evans (1988). Exact Rayleigh scattering calculations for use with the Nimbus-7 coastal zone color scanner. *Applied Optics*, 27, 862.

Gordon, H.R., D.K. Clark, J.W. Brown, O.B. Brown, R.H. Evans, and W.W. Broenkow (1983). Phytoplankton pigment concentrations in the Middle Atlantic Bight: comparison between ship determinations and Coastal Zone Color Scanner estimates. *Applied Optics*, 22, 20.

Gordon, H.R., and A.Y. Morel (1983). *Remote Assessment of Ocean Color for Interpretation of Satellite Visible Imagery: A Review*. New York: Springer-Verlag, p. 114.

Gordon, H.R., and M. Wang (1992). Surface roughness considerations for atmospheric correction of ocean color sensors. 1. The Rayleigh scattering component. *Applied Optics*, 31, 4247.

Gordon, H.R., and M. Wang (1994a). Retrieval of water-leaving radiance and aerosol optical thickness over the oceans with SeaWiFS: a preliminary algorithm. *Applied Optics*, 33, 443.

Gordon, H.R., and M. Wang (1994b). Influence of oceanic whitecaps on atmospheric correction of SeaWiFS. *Applied Optics*, 33, 7754.

Herring, David. (1997). Marine optical buoy (MOBY) Evolves, while marine optical characterization experiment (MOCE) continues in support of SeaWiFS, MODIS, and OCTS, The Earth Observer, Vol. 9, No. 5, 15-20.

Hu, C., K. Carder, F. Muller-Karger (1999). Atmospheric correction of SeaWiFS imagery over turbid coastal water (private communication).

Hucks, J. (1998). RSTX Internal Memorandum Y1629.

Koepke, P. (1984). Effective Reflectance of Oceanic Whitecaps. *Applied Optics*, 23, 1816.

Ladner, S.D., R.W. Gould, R.A. Arnone, and P.M. Martinolich (1998). Comparison of ship and SeaWiFS-derived reflectances and inherent optical properties. In *Proceedings of the Fifth International Conference on Remote Sensing for Marine and Coastal Environments*, Vol. I, p. 449.

Liu, Q., and E. Ruprecht (1996). A radiative transfer model: matrix operator method. *Appli. Opt*., 35, 4229-4237.

McClain, C.R., W.E. Esaias, W. Barnes, B. Guenther, D. Endres, S.B. Hooker, B.G. Mitchell, and R. Barnes (1992). SeaWiFS calibration and validation plan. *SeaWiFS Technical Report Series*, Vol. 3.

McClain, C.R., Eueng-Nan Yeh, (1994). Sun Glint Flag Sensitivity Study. *SeaWiFS Technical Report Series*, Vol. 13, NASA Technical Memorandum 104566.

Morel, A. (1988). Optical modelling of the upper ocean in relation to its biogenous matter content (Case 1 waters). *J. Geophys. Res*., 93, 10749.

Mueller, J.L., and R.W. Austin (1995). Ocean optics protocols for SeaWiFS validation, Revision 1. NASA Tech. Memo. 104566, Vol. 25, S. B. Hooker and E. R. Firestone, Eds., NASA Goddard Space Flight Center.

Odegard N. and Vasilkov A.P. 1998, Raytheon ITSS Document RAD.NEDL.OC.

O'Reilly J.E., Maritorena S., Mitchell B.G., Siegel D.A., Carder K.L., Garver S.A., Kahru M., and McClain C. 1998, "Ocean color chlorophyll algorithms for SeaWiFS", *J. Geophys. Res*, 103, pp. 24,937-24,953.

Robins, D.B., A.J. Bale, G.F. Moore, N.W. Rees, S.B. Hooker, C.P. Gallienne, A.G. Westbrook, E. Maranon, W.H. Spooner, and S.R. Laney (1996). AMT-1 cruise report and preliminary results. NASA Tech. Memo. 104566, Vol. 35. S.B. Hooker and E.R. Firestone, Eds., NASA Goddard Space Flight Center.

Shettle, E.P., and R.W. Fenn (1979). Models for the aerosols of the lower atmosphere and the effects of humidity variations on their optical properties. Air Force Geophys. Lab., Hanscom AFB, MA, AFGL-TR-79-0214.

Stumpf, R.P., V. Ransibrahmanakul, R.A. Arnone, K. Carder, D. Steward, J.R. Pennock, P.A. Tester, M.L. Frayer, and C. Tomas (1998). SeaWiFS ocean color algorithms for turbid coastal waters of the U.S. southeast. In *Proceedings of the Fifth International Conference on Remote Sensing for Marine and Coastal Environments*, Vol. I, p. 141.

Tassan, S. (1994) "Local algorithms using SeaWiFS data for the retrieval of phytoplankton pigments, suspended sediment, and yellow substance in coastal waters," *Appl. Opt.*, Vol. 33, 2369-2378.

Vasilkov A.P. 1999, Raytheon ITSS Document CAL.ARA.OC.

Vasilkov A.P., V.I. *Burenkov*, and K.G. Ruddick (1998). The spectral reflectance and transparency of river plume waters. *International Journal of Remote Sensing*, 20, pp. 2497-2508.